arXiv:1303.5979v1 [hep-lat] 24 Mar 2013

Nucleon form factors and moments of generalized parton distributions using $N_f = 2 + 1 + 1$ twisted mass fermions

C. Alexandrou [(a,b)], M. Constantinou [(a)], S. Dinter [(c)], V. Drach [(c)], K. Jansen [(a,c)], C. Kallidonis [(a)], G. Koutsou[(b)]

[(a)] *Department of Physics, University of Cyprus, P.O. Box 20537, 1678 Nicosia, Cyprus*

[(b)] *Computation-based Science and Technology Research Center, Cyprus Institute, 20 Kavafi Str., 2121 Nicosia, Cyprus*

[(c)] *NIC, DESY, Platanenallee 6, D-15738 Zeuthen, Germany*

We present results on the axial and the electromagnetic form factors of the nucleon, as well as, on the first moments of the nucleon generalized parton distributions using maximally twisted mass fermions. We analyze two N_f=2+1+1 ensembles having pion masses of 10 MeV and 354 MeV at two values of the lattice spacing. The lattice scale is determined using the nucleon mass computed on a total of 18 N_f=2+1+1 ensembles generated at three values of the lattice spacing, a. The renormalization constants are evaluated non-perturbatively with a perturbative subtraction of $\mathcal{O}(a^2)$-terms. The moments of the generalized parton distributions are given in the $\overline{\text{MS}}$ scheme at a scale of $\mu = 2$ GeV. We compare with recent results obtained using different discretization schemes. The implications on the spin content of the nucleon are also discussed.

PACS numbers: 11.15.Ha, 12.38.Gc, 12.38.Aw, 12.38.-t, 14.70.Dj

I. INTRODUCTION

Recent progress in the numerical simulation of Lattice Quantum Chromodynamics (LQCD) has been remarkable. The improvements in the algorithms used and the increase in computational power have enabled simulations to be carried out at near physical parameters of the theory. This opens up exciting possibilities for *ab initio* calculation of experimentally measured quantities, as well as, for predicting quantities that are not easily accessible to experiment. Understanding nucleon structure from first principles is considered a milestone of hadronic physics and a rich experimental program has been devoted to its study, starting with the measurements of the electromagnetic form factors initiated more than 50 years ago. Reproducing these key observables within the LQCD formulation is a prerequisite to obtaining reliable predictions on observables that explore Physics beyond the standard model.

A number of major collaborations have been studying nucleon structure within LQCD for many years. However, it is only recently that these quantities can be obtained with near physical parameters both in terms of the value of the pion mass, as well as, with respect to the continuum limit [1–11]. The nucleon electromagnetic form factors are a well suited experimental probe for studying nucleon structure and thus provide a valuable benchmark for LQCD. The nucleon form factors connected to the axial-vector current are more difficult to measure and therefore less accurately known than its electromagnetic form factors. A notable exception is the nucleon axial charge, g_A, which is accurately measured in β-decays. The fact that g_A can be extracted at zero momentum transfer and that it is technically straight forward to be computed in LQCD, due to its isovector nature, makes it an ideal benchmark quantity for LQCD. The Generalized Parton Distributions (GPDs) encode information related to nucleon structure that complements the information extracted from form factors [12–14]. They enter in several physical processes such as Deeply Virtual Compton Scattering and Deeply Virtual Meson Production. Their forward limit coincides with the usual parton distributions and, using Ji's sum rule [15], allows one to determine the contribution of a specific parton to the nucleon spin. In the context of the "proton spin puzzle", which refers to the unexpectedly small fraction of the total spin of the nucleon carried by quarks, this has triggered intense experimental activity [16–20].

II. LATTICE EVALUATION

In this work we consider the nucleon matrix elements of the vector and axial-vector operators

$$\mathcal{O}_{V^a}^{\mu_1\cdots\mu_n} = \bar{\psi}\gamma^{\{\mu_1} i\overleftrightarrow{D}^{\mu_2}\ldots i\overleftrightarrow{D}^{\mu_n\}}\frac{\tau^a}{2}\psi \quad (1)$$

$$\mathcal{O}_{A^a}^{\mu_1\cdots\mu_n} = \bar{\psi}\gamma^{\{\mu_1} i\overleftrightarrow{D}^{\mu_2}\ldots i\overleftrightarrow{D}^{\mu_n\}}\gamma_5\frac{\tau^a}{2}\psi \quad (2)$$

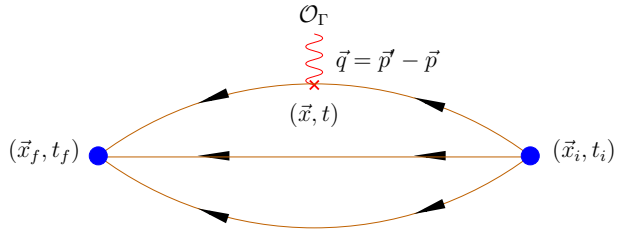

FIG. 1: Connected nucleon three-point function.

where τ^a are the Pauli matrices acting in flavor space, ψ denotes the quark doublet with components the up- and down-quarks. In this work we consider the isovector combination by taking $a = 3$, except when we discuss the spin fraction carried by each quark. Furthermore, we limit ourselves to $n = 1$ and $n = 2$. The case $n = 1$ reduces to the nucleon form factors of the vector and axial-vector currents, while $n = 2$ correspond to matrix elements of operators with a single derivative. The curly brackets represent a symmetrization over indices and subtraction of traces, only applicable to the operators with derivatives. There are well developed methods to compute the so called connected diagram, depicted in Fig. 1, contributing to the matrix elements of these operators in LQCD. Each operator can be decomposed in terms of generalized form factors (GFFs) as follows: The matrix element of the local vector current, $\mathcal{O}^\mu_{V^3}$, is expressed as a function of the Dirac and Pauli form factors

$$\langle N(p',s')|\mathcal{O}^\mu_{V^3}|N(p,s)\rangle = \bar{u}_N(p',s')\left[\gamma^\mu F_1(q^2) + \frac{i\sigma^{\mu\nu}q_\nu}{2m_N}F_2(q^2)\right]\frac{1}{2}u_N(p,s) \quad ,$$

where $u_N(p,s)$ denote the nucleon spinors of a given momentum p and spin s. $F_1(0)$ measures the nucleon charge while $F_2(0)$ measures the anomalous magnetic moment. They are connected to the electric, G_E, and magnetic, G_M, Sachs form factors by the relations

$$\begin{aligned} G_E(q^2) &= F_1(q^2) + \frac{q^2}{(2m_N)^2}F_2(q^2) \\ G_M(q^2) &= F_1(q^2) + F_2(q^2)\,. \end{aligned} \tag{3}$$

The local axial current matrix element of the nucleon $\langle N(p',s')|\mathcal{O}^\mu_{A^3}|N(p,s)\rangle$ can be expressed in terms of the form factors G_A and G_p as

$$\langle N(p',s')|\mathcal{O}^\mu_{A^3}|N(p,s)\rangle = \bar{u}_N(p',s')\left[G_A(q^2)\gamma_\mu\gamma_5 + \frac{q_\mu\gamma_5}{2m_N}G_p(q^2)\right]\frac{1}{2}u_N(p,s)\,. \tag{4}$$

The matrix elements of the one derivative operators are parameterized in terms of the GFFs $A_{20}(q^2)$, $B_{20}(q^2)$, $C_{20}(q^2)$, and $\tilde{A}_{20}(q^2)$ and $\tilde{B}_{20}(q^2)$ for the vector and axial-vector operators respectively, according to

$$\langle N(p',s')|\mathcal{O}^{\mu\nu}_{V^3}|N(p,s)\rangle = \bar{u}_N(p',s')\left[A_{20}(q^2)\,\gamma^{\{\mu}P^{\nu\}} + B_{20}(q^2)\,\frac{i\sigma^{\{\mu\alpha}q_\alpha P^{\nu\}}}{2m} + C_{20}(q^2)\,\frac{1}{m}q^{\{\mu}q^{\nu\}}\right]\frac{1}{2}u_N(p,s)\,, \tag{5}$$

$$\langle N(p',s')|\mathcal{O}^{\mu\nu}_{A^3}|N(p,s)\rangle = \bar{u}_N(p',s')\left[\tilde{A}_{20}(q^2)\,\gamma^{\{\mu}P^{\nu\}}\gamma^5 + \tilde{B}_{20}(q^2)\,\frac{q^{\{\mu}P^{\nu\}}}{2m}\gamma^5\right]\frac{1}{2}u_N(p,s)\,. \tag{6}$$

Note that the GFFs depend only on the momentum transfer squared, $q^2 = (p'-p)^2$, p' is the final and p the initial momentum. The isospin limit corresponds to taking $\tau^3/2$ in Eq. (2) and gives the form factor of the proton minus the form factors of the neutron. In the forward limit we thus have $G_E(0) = 1$ and $G_M(0) = \mu_p - \mu_n - 1 = 3.7$ [21], which is the isovector anomalous magnetic moment. Similarly, we obtain the nucleon axial charge, $G_A(0) \equiv g_A$, the isovector momentum fraction, $A_{20}(0) \equiv \langle x\rangle_{u-d}$ and the moment of the polarized quark distribution, $\tilde{A}_{20}(0) \equiv \langle x\rangle_{\Delta u - \Delta d}$. In order, to find the spin and angular momentum carried by each quark individually in the nucleon we need the isoscalar axial charge and the isoscalar one-derivative matrix elements of the vector operator. Unlike the isovector combinations, where disconnected fermion loops vanish in the continuum limit, the isoscalar cases receive contributions from disconnected fermion loops. These contributions are believed to be small and are usually neglected. Their evaluation is difficult due to the computational cost but techniques are being developed to compute them [22]. If one assumes that the disconnected contributions are small, it is straightforward to evaluate the isoscalar matrix elements taking into account only the connected part depicted in Fig. 1. The quark contribution to the nucleon spin is obtained using Ji's sum rule: $J^q = \frac{1}{2}[A^q_{20}(0) + B^q_{20}(0)]$. Moreover, using the axial charge for each quark, g^q_A, we obtain the intrinsic spin

of each quark, $\Delta\Sigma^q = g_A^q$, and via the decomposition $J^q = \frac{1}{2}\Delta\Sigma^q + L^q$ we can extract the quark orbital angular momentum L^q.

In the present work we employ the twisted mass fermion (TMF) action [23] and the Iwasaki improved gauge action [24]. Twisted mass fermions provide an attractive formulation of lattice QCD that allows for automatic $\mathcal{O}(a)$ improvement, infrared regularization of small eigenvalues and fast dynamical simulations [25]. In the computation of GFFs the automatic $\mathcal{O}(a)$ improvement is particularly relevant since it is achieved by tuning only one parameter in the action, requiring no further improvements on the operator level.

We use the twisted mass Wilson action for the light doublet of quarks

$$S_l = \sum_x \bar{\chi}_l(x) \left[D_W + m_{(0,l)} + i\gamma_5\tau^3\mu_l\right] \chi_l(x)\,, \qquad (7)$$

where D_W is the Wilson Dirac operator, $m_{(0,l)}$ is the untwisted bare quark mass, μ_l is the bare light twisted mass. The quark fields χ_l are in the so-called "twisted basis" obtained from the "physical basis" at maximal twist by the transformation

$$\psi = \frac{1}{\sqrt{2}}[\mathbf{1} + i\tau^3\gamma_5]\chi_l \quad \text{and} \quad \bar{\psi} = \bar{\chi}_l \frac{1}{\sqrt{2}}[\mathbf{1} + i\tau^3\gamma_5]\,. \qquad (8)$$

In addition to the light sector, we introduce a twisted heavy mass-split doublet $\chi_h = (\chi_c, \chi_s)$ for the strange and charm quarks, described by the action

$$S_h = \sum_x \bar{\chi}_h(x) \left[D_W + m_{(0,h)} + i\gamma_5\tau^1\mu_\sigma + \tau^3\mu_\delta\right] \chi_h(x)\,, \qquad (9)$$

where $m_{(0,h)}$ is the untwisted bare quark mass for the heavy doublet, μ_σ is the bare twisted mass along the τ^1 direction and μ_δ is the mass splitting in the τ^3 direction. The quark mass $m_{(0,h)}$ is set equal to $m_{(0,l)}$ in the simulations thus ensuring $\mathcal{O}(a)$-improvement also in the heavy quark sector. The chiral rotation for the heavy quarks from the twisted to the physical basis is

$$\psi = \frac{1}{\sqrt{2}}[\mathbf{1} + i\tau^1\gamma_5]\chi_h \quad \text{and} \quad \bar{\psi} = \bar{\chi}_h \frac{1}{\sqrt{2}}[\mathbf{1} + i\tau^1\gamma_5]\,. \qquad (10)$$

The reader can find more details on the twisted mass fermion action in Ref. [26].

A. Correlation functions

The GFFs are extracted from dimensionless ratios of correlation functions, involving two-point and three-point functions that are defined by

$$G(\vec{q}, t_f - t_i) = \sum_{\vec{x}_f} e^{-i(\vec{x}_f - \vec{x}_i)\cdot\vec{q}}\, \Gamma^0_{\beta\alpha} \left\langle J_\alpha(t_f, \vec{x}_f)\overline{J}_\beta(t_i, \vec{x}_i)\right\rangle \qquad (11)$$

$$G^{\mu_1\cdots\mu_n}(\Gamma^\nu, \vec{q}, t) = \sum_{\vec{x}, \vec{x}_f} e^{i(\vec{x} - \vec{x}_i)\cdot\vec{q}}\, \Gamma^\nu_{\beta\alpha} \left\langle J_\alpha(t_f, \vec{x}_f)\mathcal{O}^{\mu_1\cdots\mu_n}(t, \vec{x})\overline{J}_\beta(t_i, \vec{x}_i)\right\rangle . \qquad (12)$$

For the insertion, $\mathcal{O}^{\mu_1\cdots\mu_n}$, we employ the vector $(\bar{\psi}\,\gamma^\mu\psi)$, the axial-vector $(\bar{\psi}\,\gamma^5\,\gamma^\mu\psi)$, the one-derivative vector $(\bar{\psi}\,\gamma^{\{\mu_1}D^{\mu_2\}}\psi)$ and the one-derivative axial-vector $(\bar{\psi}\,\gamma 5\,\gamma^{\{\mu_1}D^{\mu_2\}}\psi)$ operators. We consider kinematics for which the final momentum $\vec{p}' = 0$ and in our approach we fix the time separation between sink and source $t_f - t_i$. The projection matrices Γ^0 and Γ^k are given by

$$\Gamma^0 = \frac{1}{4}(\mathbb{1} + \gamma_0)\,, \quad \Gamma^k = \Gamma^0 i\gamma_5\gamma_k\,. \qquad (13)$$

The proton interpolating field written in terms of the quark fields in the twisted basis ($\tilde{u}$ and $\tilde{d}$) at maximal twist is given by

$$J(x) = \frac{1}{\sqrt{2}}[\mathbb{1} + i\gamma_5]\epsilon^{abc}\left[\tilde{u}^{a\top}(x)\mathcal{C}\gamma_5\tilde{d}^b(x)\right]\tilde{u}^c(x)\,, \qquad (14)$$

where $\mathcal{C}$ is the charge conjugation matrix. We use Gaussian smeared quark fields [27, 28] to increase the overlap with the proton state and decrease overlap with excited states. The smeared interpolating fields are given by

$$\begin{aligned} q^a_{\rm smear}(t, \vec{x}) &= \sum_{\vec{y}} F^{ab}(\vec{x}, \vec{y}; U(t))\; q^b(t, \vec{y})\,, \qquad (15)\\ F &= (\mathbb{1} + a_G H)^{N_G}\,,\\ H(\vec{x}, \vec{y}; U(t)) &= \sum_{i=1}^{3}[U_i(x)\delta_{x,y-\hat{\imath}} + U_i^\dagger(x - \hat{\imath})\delta_{x,y+\hat{\imath}}]\,. \end{aligned}$$

We also apply APE-smearing to the gauge fields U_μ entering the hopping matrix H. The parameters for the Gaussian smearing a_G and N_G are optimized using the nucleon ground state [29]. Different combination of Gaussian parameters, $N_{\rm G}$ and $a_{\rm G}$, have been tested and it was found

that combinations of N_G and a_G that give a root mean square radius of about 0.5 fm are optimal for suppressing excited states. The results of this work have been produced with

$$\beta = 1.95: \;\; N_G = 50\,,\; a_G = 4,\; N_{\rm APE} = 20,\; a_{\rm APE} = 0.5,$$
$$\beta = 2.10: \;\; N_G = 110,\; a_G = 4,\; N_{\rm APE} = 50,\; a_{\rm APE} = 0.5\,.$$

As already point out, in correlators of isovector operators the disconnected diagrams are zero up to lattice artifacts, and can be safely neglected as we approach the continuum limit. Thus, these correlators can be calculated by evaluating the connected diagram of Fig. 1 for which we employ sequential inversions through the sink [30]. The creation operator is taken at a fixed position $\vec{x}_i$=$\vec{0}$ (source). The annihilation operator at a later time t_f (sink) carries momentum $\vec{p}$=0. The current couples to a quark at an intermediate time t and carries momentum $\vec{q}$. Translation invariance enforces $\vec{q} = -\vec{p}$ for our kinematics. At a fixed sink-source time separation we obtain results for all possible momentum transfers and insertion times as well as for any operator $\mathcal{O}_\Gamma^{\{\mu_1\cdots\mu_n\}}$, with one set of sequential inversions per choice of the sink. We perform separate inversions for the two projection matrices Γ^0 and $\sum_k \Gamma^k$ given in Eq. (13). An alternative approach that computes the spatial all-to-all propagator stochastically has shown ot be suitable for the evaluation of nucleon three-point functions [31]. Within this approach one can include any projection without needing additional inversions.

Using the two- and three-point functions of Eqs. (11)-(12) and considering operators with up to one derivative we form the ratio

$$R^{\mu\nu}(\Gamma^\lambda,\vec{q},t) \;=\; \frac{G^{\mu\nu}(\Gamma^\lambda,\vec{q},t)}{G(\vec{0},t_f-t_i)} \times\sqrt{\frac{G(\vec{p},t_f-t)G(\vec{0},t-t_i)G(\vec{0},t_f-t_i)}{G(\vec{0},t_f-t)G(\vec{p},t-t_i)G(\vec{p},t_f-t_i)}}\,, \quad (16)$$

which is optimized because it does not contain potentially noisy two-point functions at large separations and because correlations between its different factors reduce the statistical noise. For sufficiently large separations $t_f - t$ and $t - t_i$ this ratio becomes time-independent (plateau region):

$$\lim_{t_f-t\to\infty}\lim_{t-t_i\to\infty} R^{\mu\nu}(\Gamma^\lambda,\vec{q},t) = \Pi^{\mu\nu}(\Gamma^\lambda,\vec{q})\,. \quad (17)$$

From the plateau values of the renormalized asymptotic ratio $\Pi(\Gamma^\lambda,\vec{q})_R = Z\,\Pi(\Gamma^\lambda,\vec{q})$ the nucleon matrix elements of all our operators can be extracted. The equations relating $\Pi(\Gamma^\lambda,\vec{q})$ to the GFFs can be found in Refs. [1–3]. All values of $\vec{q}$ resulting in the same q^2, the two choices of projector matrices Γ^0 and $\sum_k \Gamma^k$ given Eq. (13) and the relevant orientations μ,ν of the operators lead to an over-constrained system of equations, which is solved in the least-squares sense via a singular value decomposition of the coefficient matrix. All quantities will be given in Euclidean space with $Q^2 \equiv -q^2$ the Euclidean momentum transfer squared. Both projectors Γ^0 and $\sum_k \Gamma^k$ are required to obtain all GFFs, except for the case of the local axial-vector operator, for which the projection with Γ^0 leads to zero. For the one derivative vector operator, both cases $\mu = \nu$ and $\mu \neq \nu$ are necessary to extract all three GFFs, which on a lattice renormalize differently from each other [32]. On the other hand, the one-derivative axial-vector form factors can be extracted using only correlators with $\mu \neq \nu$, but we use all combinations of μ,ν in order to increase statistics. In Fig. 2 we show representative plateaus for the ratios of the local axial-vector and the one derivative vector operators at $\beta = 1.95$, using different momenta, projectors, and indices μ, ν.

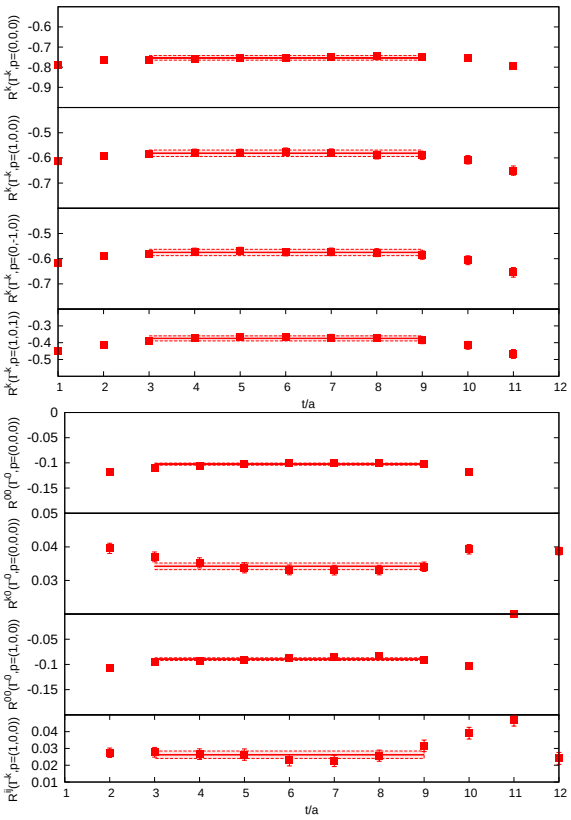

FIG. 2: Ratios for the matrix elements of the local axial-vector operator (upper) and one derivative vector operator (lower) for a few exemplary choices of the momentum. The solid lines with the bands indicate the fitted plateau values with their jackknife errors. From top to bottom the momentum takes values $\vec{p} = (0,0,0)$, $(1,0,0)$, $(0,-1,0)$ and $(1,0,1)$.

Since we use sequential inversions through the sink we need to fix the sink-source separation. Optimally, one wants to keep the statistical errors on the ratio of Eq. (16) as small as possible by using the smallest value for the sink-source time separation that still ensures that the excited state contributions are sufficiently suppressed. Recent studies have shown that the optimal sink-source sep-

aration is operator dependent [33, 34]. For g_A excited state contamination was found to be small. We have also tested different values of the sink-source time separation [3] for the magnetic form factor and found consistent results when the sink-source separation was about 1 fm within our statistical accuracy. For the momentum fraction one would need to re-examine the optimal sink-source separation, which would require a dedicate high accuracy study. Since in this work we are computing several observables, we will we use $t_f - t_i \sim 1$ fm that correspond to the following values

$$\beta = 1.95 : (t_f - t_i)/a{=}12\,, \quad \beta = 2.10 : (t_f - t_i)/a{=}18.$$

This choice allows to compare with other lattice QCD results where similar values were used.

B. Simulation details

In Table I we tabulate the input parameters of the calculation, namely β, L/a and the light quark mass $a\mu$, as well as, the value of the pion mass in lattice units [35, 36]. The strange and charm quark masses were fixed to approximately reproduce the physical kaon and D-meson masses, respectively [37]. The lattice spacing a given in this Table is determined from the nucleon mass as explained in the following subsection and it will be used for the baryon observables discussed in this paper. We note that the study of the systematic error in the scale setting using the pion decay constant as compared to the value extracted using the nucleon mass is currently being pursued. Since the GFFs are dimensionless they are not affected by the scale setting. However, a is needed to convert Q^2 to physical units and therefore it does affect quantities like the anomalous magnetic moment and Dirac and Pauli radii since these are dimensionful parameters and depend on fitting the Q^2-dependence of the form factors.

$\beta = 1.95$, $a = 0.0863(11)$ fm, $r_0/a = 5.66(3)$		
$32^3 \times 64$, $L = 2.5$ fm	$a\mu$	0.0055
	No. of confs	950
	$a\,m_\pi$	0.15518(21)(33)
	Lm_π	4.97
$\beta = 2.10$, $a = 0.0657(7)$ fm, $r_0/a = 7.61(6)$		
$48^3 \times 96$, $L = 2.9$ fm	$a\mu$	0.0015
	No. of confs	900
	$a\,m_\pi$	0.06975(20)
	Lm_π	3.35

TABLE I: Input parameters $(\beta, L, a\mu)$ of our lattice calculation with the corresponding lattice spacing a, determined from the nucleon mass, and pion mass am_π in lattice units.

C. Determination of lattice spacing

For the observables discussed in this work the nucleon mass at the physical point is the most appropriate quantity to set the scale. The values for the nucleon mass were computed using N_f=2+1+1 ensembles for β=1.90, β=1.95 and β=2.10, a range of pion masses and volumes. To extract the mass we consider the two-point correlators defined in Eq. (11) and construct the effective mass

$$\begin{aligned} a\,m_N^{\rm eff}(t) &= -\log(C(t)/C(t-1)) \\ &= a\,m_N + \log\Big(\frac{1+\sum_{j=1}^{\infty} c_j e^{-\Delta_j t}}{1+\sum_{j=1}^{\infty} c_j e^{-\Delta_j (t-1)}}\Big) \\ &\xrightarrow{t\to\infty} a\,m_N \end{aligned} \tag{18}$$

where $\Delta_j = E_j - m_N$ is the energy difference of the excited state j with respect to the ground state mass, m_N. Our fitting procedure to extract m_N is as follows: The mass is obtained from a constant fit to $m_N^{\rm eff}(t)$ for $t \geq t_1$ for which the contamination of excited states is believed to be small. We denote the value extracted as $m_N^{(A)}(t_1)$. A second fit to $m_N^{\rm eff}(t)$ is performed including the first excited state for $t \geq t_1'$, where t_1' is taken to be $2a$ or $3a$. We denote the value for the ground state mass extracted from the fit to two exponentials $m_N^{(B)}$. We vary t_1 such that the ratio

$$\frac{|a\,m_N^{(A)}(t_1) - a\,m_N^{(B)}|}{a\,m_N^{mean}}, \quad \text{where}$$
$$a\,m_N^{mean} = \frac{a\,m_N^{(A)}(t_1) + a\,m_N^{(B)}}{2} \tag{19}$$

drops below 50% of the statistical error on $m_N^A(t_1)$. The resulting values for the nucleon mass are collected in Table II.

In Fig. 3 we show results at three values of the lattice spacing corresponding to β=1.90, β=1.95 and β=2.10. As can be seen, cut-off effects are negligible and we can therefore use continuum chiral perturbation theory to extrapolate to the physical point using all the lattice results.

To chirally extrapolate we use the well-established $\mathcal{O}(p^3)$ result of chiral perturbation theory (χPT) given by

$$m_N = m_N^0 - 4c_1 m_\pi^2 - \frac{3g_A^2}{16\pi f_\pi^2} m_\pi^3\,. \tag{20}$$

We perform a fit to the results at the three β values given in Table II and extract

$$\begin{aligned} a_{\beta=1.90} &= 0.0950(11)(20)\,, \\ a_{\beta=1.95} &= 0.0863(9)(20)\,, \\ a_{\beta=2.10} &= 0.0657(7)(15)\,. \end{aligned} \tag{21}$$

We would like to point out that our lattice results show a curvature supporting the m_π^3-term. In order to estimate the systematic error due to the chiral extrapolation we also perform a fit using heavy baryon (HB) χPT

β	$a\mu$	Volume	am_π	statistics	am_N
1.90	0.003	$32^3\times64$	0.124	217	0.506(11)
1.90	0.004	$20^3\times48$	0.149	617	0.550(19)
1.90	0.004	$24^3\times48$	0.145	523	0.549(9)
1.90	0.004	$32^3\times64$	0.141	389	0.518(8)
1.90	0.005	$32^3\times64$	0.158	387	0.542(6)
1.90	0.006	$24^3\times48$	0.173	479	0.569(8)
1.90	0.008	$24^3\times48$	0.199	449	0.587(7)
1.90	0.010	$24^3\times48$	0.223	501	0.616(6)
1.95	0.0025	$32^3\times64$	0.107	939	0.461(5)
1.95	0.0035	$32^3\times64$	0.126	2513	0.488(3)
1.95	0.0055	$32^3\times64$	0.155	1413	0.513(3)
1.95	0.0075	$32^3\times64$	0.180	1109	0.532(4)
1.95	0.0085	$24^3\times48$	0.194	937	0.542(5)
2.10	0.0015	$48^3\times96$	0.070	1002	0.338(4)
2.10	0.0020	$48^3\times96$	0.080	186	0.351(7)
2.10	0.0030	$48^3\times96$	0.098	226	0.362(7)
2.10	0.0045	$32^3\times64$	0.121	1905	0.394(3)

TABLE II: Values of the nucleon mass and the associated statistical error.

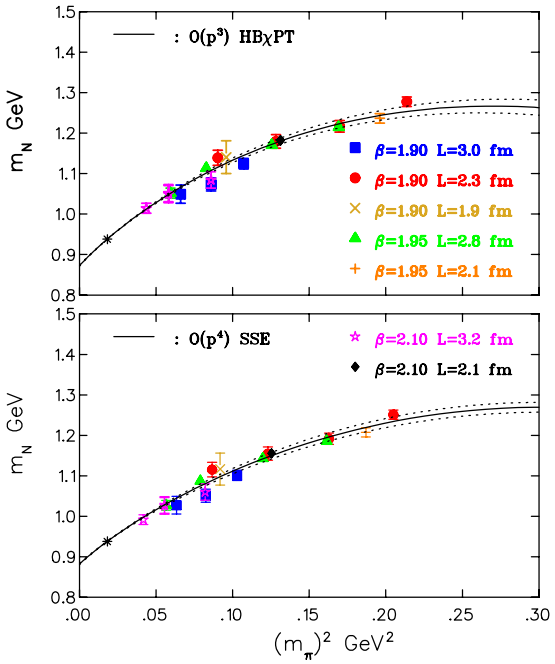

FIG. 3: Nucleon mass at three lattice spacings. The solid lines are fits to $\mathcal{O}(p^3)$ and $\mathcal{O}(p^4)$ HBχPT with explicit Δ degrees of freedom in the so called small scale expansion(SSE). The dotted lines denote the error band. The physical point is shown with the asterisk.

to $\mathcal{O}(p^4)$ with explicit Δ degrees of freedom in the so called small scale expansion(SSE) [29]. We take the difference between the $\mathcal{O}(p^3)$ and $\mathcal{O}(p^4)$ mean values as an estimate of the uncertainty due to the chiral extrapolation. This error is given in the second parenthesis in Eqs. (21) and it is about twice the statistical error. The values of the lattice spacing given in Eqs. (21) will be used for converting to physical units the quantities we study here. We would like to point out that redoing the $\mathcal{O}(p^3)$ fit eliminating data for which $Lm_\pi < 3.5$ yields $a_{\beta=1.90} = 0.0942(14)$ fm, $a_{\beta=1.95} = 0.0858(11)$ fm and $a_{\beta=2.1} = 0.0653(8)$, which are consistent with the values given in Eq. (21). In performing these fits we only take into account statistical errors. Systematic errors due to the choice of the plateau are not included. We also note that the lattice spacings were also determined from the pion decay constant using NLO SU(2) chiral perturbation theory to extrapolate the lattice data. The values obtained at $\beta = 1.90$, 1.95 and 2.10 in this preliminary analysis that included only a subset of the ensembles used here are smaller [36], as compared to the values extracted using the nucleon mass. For the two β-values studied in this work they were found to be $a_{f_\pi} = 0.0779(4)$ fm at $\beta = 1.95$ and $a_{f_\pi} = 0.0607(3)$ fm at $\beta = 2.10$, where with a_{f_π} we denote the lattice spacing determined using the pion decay constant. This means that the values of the pion mass in physical units quoted in this paper are equivalently smaller than those obtained using a_{f_π} to convert to physical units. A comprehensive analysis of the scale setting and the associated systematic uncertainties is currently being carried out by European Twisted Mass Collaboration (ETMC) and will appear elsewhere.

D. Renormalization

We determine the renormalization constants needed for the operators discussed in this work in the RI′-MOM scheme [38] by employing a momentum source at the vertex [39]. The advantage of this method is the high statistical accuracy and the evaluation of the vertex for any operator including extended operators at no significant additional computational cost. For the details of the non-perturbative renormalization see Ref. [38]. In the RI scheme the renormalization constants are defined in the chiral limit. Since the mass of the strange and charm quarks are fixed to their physical values in these simulations, extrapolation to the chiral limit is not possible. Therefore, in order to compute the renormalization constants needed to obtain physical observables, ETMC has generated N_f=4 ensembles for the same β values so that the chiral limit can be taken [40]. Although we will use the N_f=4 ensembles for the final determination of the renormalization constants, it is also interesting to compute the renormalization constants using the N_f=2+1+1 ensembles and study their quark mass dependence. This test was performed on both the $\beta = 1.95$ and the $\beta = 2.10$ ensembles. In the upper panel of Fig. 4 we show results at $\beta = 2.10$ for both N_f=4 and N_f=2+1+1 ensembles for the one derivative Z-factors in the RI′-MOM scheme. As can be seen, we obtain compatible values for all four cases. We also observe the same agreement for Z_V and Z_A also at $\beta = 1.95$. This can be understood by examin-

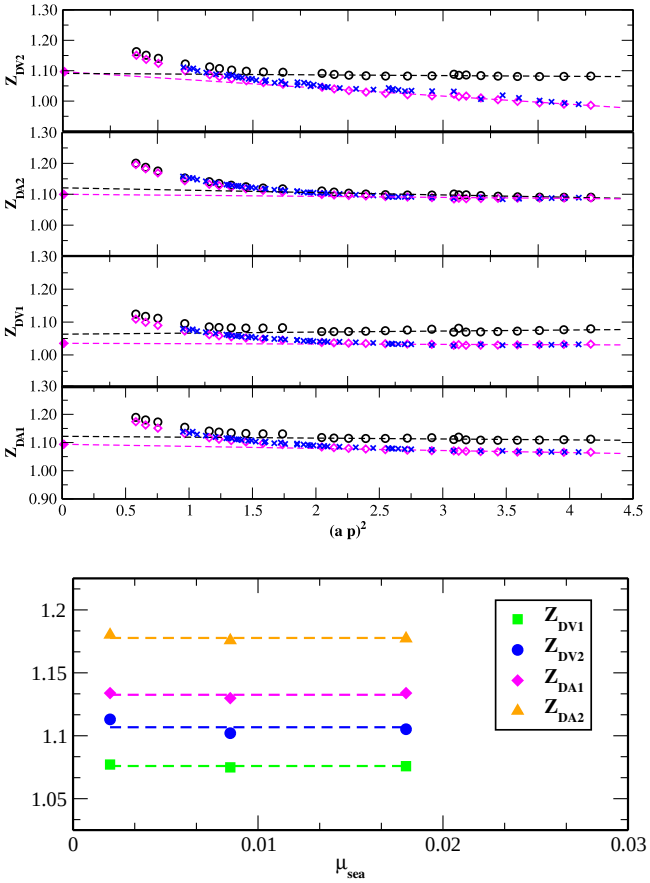

FIG. 4: Upper panel: One derivative renormalization functions for $\beta = 2.10$, $a\mu = 0.0015$ using N_f=4 gauge configurations, where $Z_{DV1}\,(Z_{DA1}) \equiv Z^{\mu\mu}_{DV}\,(Z^{\mu\mu}_{DA})$ and $Z_{DV2}\,(Z_{DA2}) \equiv Z^{\mu\neq\nu}_{DV}\,(Z^{\mu\neq\nu}_{DA})$. Black circles are the unsubtracted data and the magenta diamonds the data after subtracting the perturbative $\mathcal{O}(a^2)$-terms. For comparison, we show the subtracted data using N_f=2+1+1 gauge configurations at the same value of the quark mass and β (blue crosses). Lower panel: One derivative renormalization functions for $\beta = 1.95$ using N_f=4 gauge configurations as a function of the twisted quark mass.

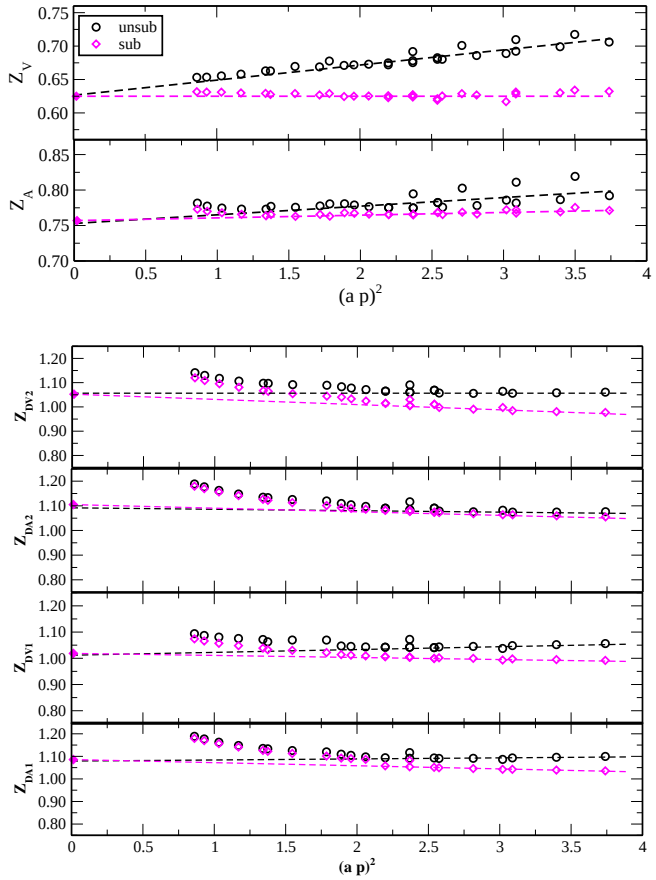

FIG. 5: Upper panel: Z_A, Z_V for $\beta = 1.95$, and $a\mu = 0.0055$; Lower panel: Renormalization constants for one derivative operators for $\beta = 1.95$, and $a\mu = 0.0055$, where $Z_{DV1}\,(Z_{DA1}) \equiv Z^{\mu\mu}_{DV}\,(Z^{\mu\mu}_{DA})$ and $Z_{DV2}\,(Z_{DA2}) \equiv Z^{\mu\neq\nu}_{DV}\,(Z^{\mu\neq\nu}_{DA})$. The lattice data are shown in black circles and the data after the $\mathcal{O}(a^2)$-terms have been subtracted are shown in magenta diamonds. The solid diamond at $(a\,p)^2 = 0$ is the value obtained after performing a linear extrapolation of the subtracted data.

ing the quark mass dependence of these renormalization constants. In the lower panel of Fig. 4 we show, for the N_f=4 case, the dependence of Z_{DV}, Z_{DA} on four light quark masses. The values we find are consistent with each other. This explains the fact that the results in the N_f=4 and N_f=2+1+1 cases are compatible. Furthermore, it makes any extrapolation of N_f=4 results to the chiral limit straight forward. We perform a perturbative subtraction of $\mathcal{O}(a^2)$-terms [38, 41, 42]. This subtracts the leading cut-off effects yielding, in general, a weak dependence of the renormalization factors on $(ap)^2$ for which the $(ap)^2 \to 0$ limit can be reliably taken, as can be seen in Figs. 4 and 5 for the two $N_f = 2+1+1$ ensembles. We also take the chiral limit, although the quark mass dependence is negligible for the aforementioned operators.

The renormalization factors for the one-derivative vector and axial-vector operators, $Z^{\mu\nu}_{DV}$ and $Z^{\mu\nu}_{DA}$, fall into different irreducible representations of the hypercubic group, depending on the choice of the external indices, μ, ν. Hence, we distinguish between $Z^{\mu\mu}_{DV}\,(Z^{\mu\mu}_{DA})$ and $Z^{\mu\neq\nu}_{DV}\,(Z^{\mu\neq\nu}_{DA})$. For the conversion factors from RI to $\overline{\rm MS}$ we used the results of Ref. [43] for the local vector and axial-vector operators while for the one-derivative operators we used the expressions of Ref. [38]. Another characteristic of these renormalization constants is that they depend on the renormalization scale. Thus, they need to be converted to the continuum $\overline{\rm MS}$-scheme, and for this we use a conversion factor computed in perturbation theory to $O(g^4)$. They are also evolved perturbatively to a reference scale, which is chosen to be $(2\ {\rm GeV})^2$. The results are shown in Fig. 5 both before subtracting the perturbative $\mathcal{O}(a^2)$-terms and after. Using the subtracted data we find the values given in Table III.

These are the values that we use in this work to renor-

	β=1.95	β=2.10
Z_V	0.625(2)	0.664(1)
Z_A	0.757(3)	0.771(2)
$Z_{DV}^{\mu\mu}$	1.019(4)	1.048(5)
$Z_{DV}^{\mu\neq\nu}$	1.053(11)	1.105(4)
$Z_{DA}^{\mu\mu}$	1.086(3)	1.112(5)
$Z_{DA}^{\mu\neq\nu}$	1.105(2)	1.119(6)

TABLE III: Renormalization constants in the chiral limit at $\beta = 1.95$ and $\beta = 2.10$ in the $\overline{\rm MS}$-scheme at $\mu = 2$ GeV.

malize the lattice matrix elements. The numbers in the parenthesis correspond to the statistical error. Our full results for the renormalization functions of the fermion field, local and one derivative bilinears along with the systematic error analysis will appear in a separate publication.

III. LATTICE RESULTS

In this section we present our results on the nucleon electromagnetic form factors, $G_E(Q^2)$ and $G_M(Q^2)$, and the axial-vector form factors, $G_A(Q^2)$ and $G_p(Q^2)$. We also show the $n = 2$ generalized form factors for the one-derivative vector operator, $A_{20}(Q^2)$, $B_{20}(Q^2)$ and $C_{20}(Q^2)$, and the one-derivative axial-vector oprator, $\tilde{A}_{20}(Q^2)$ and $\tilde{B}_{20}(Q^2)$. The numerical values are given in the Tables in Appendix A. The dependence of these quantities on the momentum transfer square, Q^2, the lattice spacing, as well as on the pion mass is examined. We also compare with recent results from other collaborations.

As we already mentioned, most of the results are obtained for isovector quantities. For the renormalized nucleon matrix element of the operators with up to one derivative we thus consider

$$\bar{u}\gamma_{\{\mu}\overleftrightarrow{D}_{\nu\}}\,u \;-\; \bar{d}\gamma_{\{\mu}\overleftrightarrow{D}_{\nu\}}\,d\,,$$
$$\bar{u}\gamma^5\,\gamma_{\{\mu}\overleftrightarrow{D}_{\nu\}}\,u \;-\; \bar{d}\gamma^5\,\gamma_{\{\mu}\overleftrightarrow{D}_{\nu\}}\,d\,,$$

in the $\overline{\rm MS}$ scheme at a scale $\mu = 2$ GeV. Note that the local vector and axial-vector operators are renormalization scale independent, thus the conversion to the $\overline{\rm MS}$ scheme is irrelevant.

In order to study the spin content of the nucleon we also compute the isoscalar matrix elements of the one-derivative vector operator, as well as, the isoscalar axial charge assuming, in all cases, that the disconnected contributions are negligible.

A. Nucleon form factors

In Fig. 6 we present our results for the axial charge $g_A \equiv G_A(0)$ using N_f=2 and N_f=2+1+1 twisted mass fermions. These are computed at different lattice spacings ranging from $a \sim 0.1$ fm to $a \sim 0.06$ fm. As can be seen, no sizable cut-off effects are observed. Lattice data computed using different volumes are also consistent down to pion masses of about 300 MeV, where we have different volumes. In a nutshell, our results do not indicate volume or cut-off effects larger than our current statistical errors. A dedicated high statistics analysis using the N_f=2+1+1 ensemble at $m_\pi = 354$ MeV has shown that contributions from excited states are negligible for g_A [33, 34]. In recent studies, the so called summation method, that sums over the time-slice t where the current is inserted, is used as an approach that better suppresses excited state contributions [44]. Using this method to analyze lattice results at near physical pion mass it was demonstrated that, in fact, the value of g_A decreases [7]. These studies thus indicate that the source of the discrepancy does not seem to come from excited states contamination.

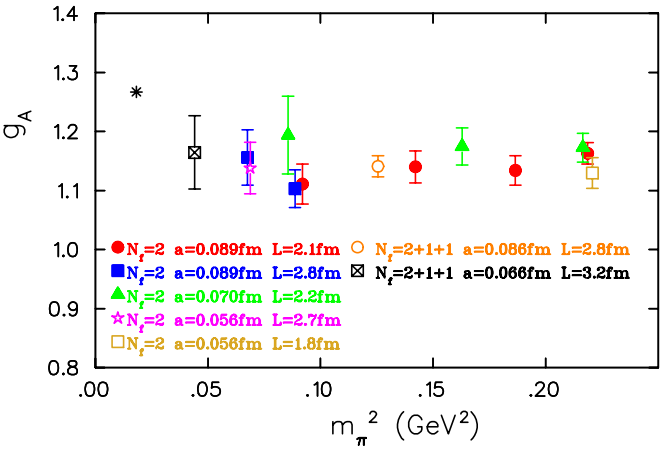

FIG. 6: Results for the nucleon axial charge with (i) N_f=2 twisted mass fermions with $a = 0.089$ fm (filled red circles for $L = 2.1$ fm and filled blue squares for $L = 2.8$ fm), $a = 0.070$ fm (filled green triangles), and $a = 0.056$ fm (open star for $L = 2.7$ fm and open square for $L = 1.8$ fm) [3] (ii) N_f=2+1+1 twisted mass fermions with $a = 0.086$ fm (open circle) and $a = 0.066$ fm (square with a cross). The asterisk is the physical value as given in the PDG [21].

In Fig. 7 we compare our results to other recent lattice QCD data obtained with different actions. We show results obtained using domain wall fermions (DWF) [5], clover fermions [48], a mixed action with 2+1 flavors of asqtad-improved staggered sea and domain wall valence fermions [45] referred to as hybrid, and N_f=2+1 of tree-level clover-improved Wilson fermions coupled to double HEX-smeared gauge fields [7, 47]. We observe that all these lattice results are compatible. This agreement corroborates the fact that cut-off effects are negligible since these lattice data are obtained with different discretized actions without being extrapolated to the continuum limit. The recent result of Ref. [47] at almost physical pion mass shows about 10% deviation from the

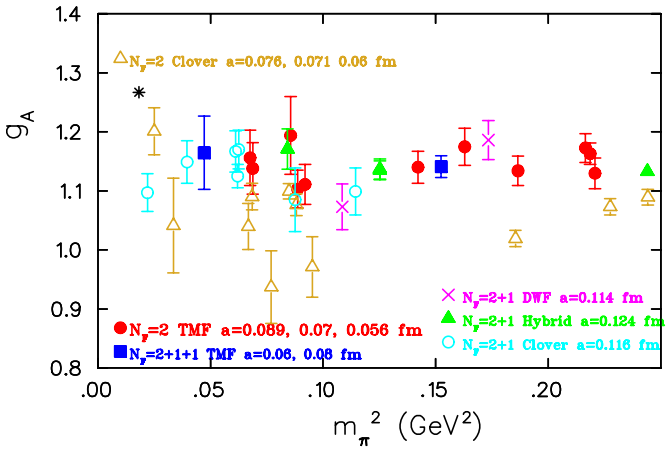

FIG. 7: The nucleon axial charge for twisted mass fermions, N_f=2 (filled red circles) and N_f=2+1+1 (filled blue squares), as well as, results using other lattice actions: Filled (green) triangles correspond to a mixed action with 2+1 flavors of staggered sea and domain wall valence fermions [45], crosses to N_f=2+1 domain wall fermions [5], open triangles to N_f=2 clover fermions [46] and open (cyan) circles to N_f=2+1 of tree-level clover-improved Wilson fermions coupled to double HEX-smeared gauge fields [47].

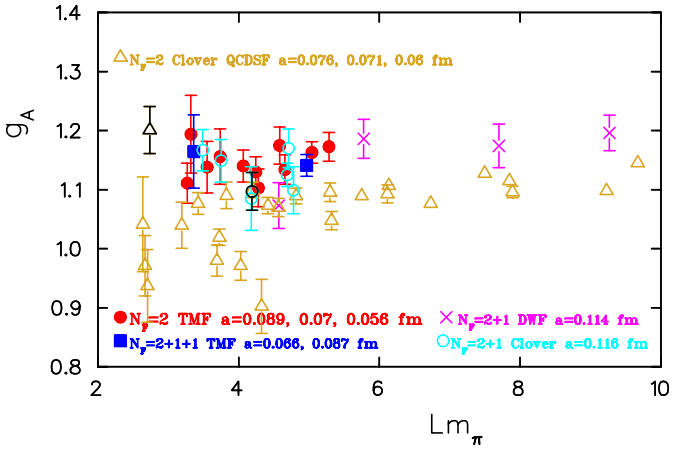

FIG. 8: The nucleon axial charge for twisted mass fermions (N_f=2 and N_f=2+1+1), as well as results using other lattice actions versus Lm_π. Black symbols denote results at almost physical pion mass obtained using N_f=2 [46] and N_f=2+1 [47] clover fermions. The rest of the notation is the same as that in Fig. 7.

physical value of $g_A^{exp} = 1.267$ [21]. This is a well-known puzzle and various directions have been explored to identify the source of the discrepancy [33, 34, 48, 49]. In Fig. 7 we also include the recent results obtained using N_f=2 clover fermions at three lattice spacings $a = 0.076$ fm, 0.071 fm and 0.060 fm [46]. They include a result at almost physical pion mass, which is clearly higher than the corresponding one obtained in Ref. [47]. As already remarked, the latter was shown to even decrease if one uses the summation method [7]. In Ref. [46] it is argued that volume corrections are sizable and increase the value of g_A. We note that all lattice data shown in Fig. 7 are not volume corrected. In order to assess, which of these results would suffer from large volume corrections we show in Fig. 8 g_A as a function of Lm_π. The data points at almost physical pion mass are shown with the black symbols. The result from Ref. [47] at $Lm_\pi = 4.2$ is lower than the one from Ref. [46] at $Lm_\pi = 2.74$. Thus volume effects alone may not account for the whole discrepancy and therefore, there is still an open issue in the evaluation of g_A.

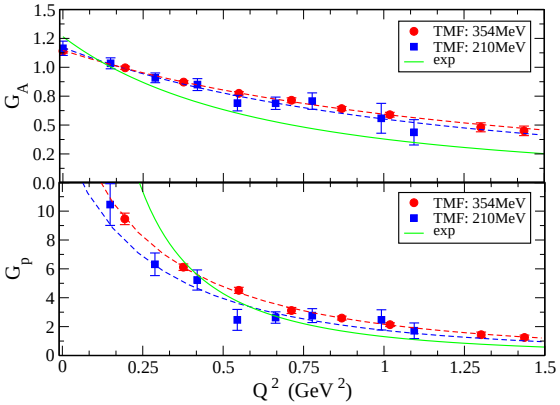

FIG. 9: Comparison of the N_f=2+1+1 twisted mass data on $G_A(Q^2)$ (upper) and $G_p(Q^2)$ (lower) for the two different pion masses considered. Filled blue squares correspond to $\beta = 2.10$ and $m_\pi = 210$ MeV, while filled red circles correspond to $\beta = 1.95$ and $m_\pi = 354$ MeV. The dashed lines are the dipole fits on the lattice data, while the solid green line is the dipole fit of experimental data for $G_A(Q^2)$ [50] in combination with pion-pole dominance for $G_p(Q^2)$.

Next, we study the dependence of the axial form factors on the momentum transfer, Q^2. In Fig. 9 we compare our N_f=2+1+1 results for $G_A(Q^2)$ and $G_p(Q^2)$ as the pion mass decreases from 354 MeV to 210 MeV. As can be seen, the dependence on the pion mass is very weak for $G_A(Q^2)$ whereas for $G_p(Q^2)$ a stronger dependence is observed in particular at low Q^2. This is not surprising since $G_p(Q^2)$ is expected to have a pion-pole dependence that dominates its Q^2-dependence as $Q^2 \to 0$. The solid line is the result of a dipole fit to the experimental electroproduction data for $G_A(Q^2)$. Assuming pion-pole dominance we can deduce from the fit to the experimental data on $G_A(Q^2)$ the expected behavior for $G_p(Q^2)$, shown in Fig. 9. As can be seen, both quantities have a smaller slope with respect to Q^2 than what is extracted from experiment. Such a behavior is common to all the nucleon form factors and it remains to be further investigated if reducing even more the pion mass will resolve this discrepancy. The Q^2-dependence of the lattice QCD data for $G_A(Q^2)$ can be well parameterized by dipole Ansatz of the form

$$G_A(Q^2) = \frac{g_A}{\left(1 + Q^2/m_A^2\right)^2}\,, \qquad (22)$$

as it was done for the experimental results. Likewise, assuming pion-pole dominance we fit $G_p(Q^2)$ to the form

$$G_p(Q^2) = \frac{G_A(Q^2)\, G_p(0)}{(Q^2 + m_p^2)}\,. \qquad (23)$$

In both fits we take into account lattice data with Q^2 up to a maximum value of $(1.5)^2$ GeV^2. The values of the parameter m_A extracted from the fit for the two ensembles are

$$\begin{aligned} \beta &= 1.95: \; m_A = 1.60(5) \text{ GeV} \\ \beta &= 2.10: \; m_A = 1.48(12) \text{ GeV}\,. \end{aligned}$$

These are higher than the experimental value of $m_A^{exp} = 1.069$ GeV [50] extracted from the best dipole parameterization to the electroproduction data. This deviation between lattice and experimental data reflects the smaller slope in the lattice QCD data. Another observation is that the fits for $G_p(Q^2)$ are strongly dependent on the lowest values of Q^2 taken in the fit due to the strong Q^2-dependence of $G_p(Q^2)$ at low Q^2.

In Figs. 10 and 11 we compare results using the two N_f=2+1+1 ensembles with those obtained with N_f=2 ensembles at similar pion masses. We do not observe large deviations between N_f=2 and N_f=2+1+1 result showing that strange and charm quark effects are small, as expected.

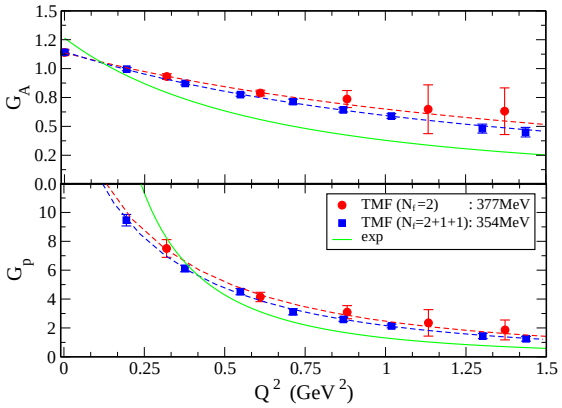

FIG. 10: The Q^2-dependence of the form factors G_A and G_p for i) N_f=2 at m_π = 377 MeV, a = 0.089 fm (filled red circles); ii) N_f=2+1+1 at m_π = 354 MeV, a = 0.086 fm. The solid line in the upper plot shows the resulting dipole fit to the experimental data on $G_A(Q^2)$ [50]. Assuming a pion-pole dependence for $G_p(Q^2)$ and using the fit on $G_A(Q^2)$ shown in the upper panel produces the solid line shown in the lower panel for $G_p(Q^2)$.

It is interesting to compare our TMF results to those obtained using different fermion discretization schemes. We collect recent lattice QCD results in Figs. 12 and 13 at similar pion masses. As can be seen, in the case of $G_A(Q^2)$ there is agreement of our results with those obtained using DWF and the hybrid approach. For $G_p(Q^2)$ hybrid results obtained on a larger volume are higher at

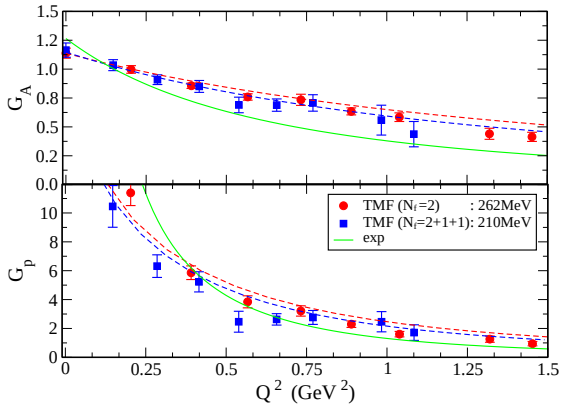

FIG. 11: The Q^2-dependence of the form factors G_A (upper) and G_p (lower) for N_f=2+1+1 twisted mass fermions at m_π = 210 MeV, a = 0.066 fm (filled blue squares) and N_f=2 twisted mass fermions at m_π = 262 MeV and a = 0.056 fm (filled red circles). The rest of the notation is the same as that in Fig. 10.

small Q^2-values. This is an indication that volume effects are larger for quantities like $G_p(Q^2)$ for which pion cloud effects are expected to be particularly large at small Q^2.

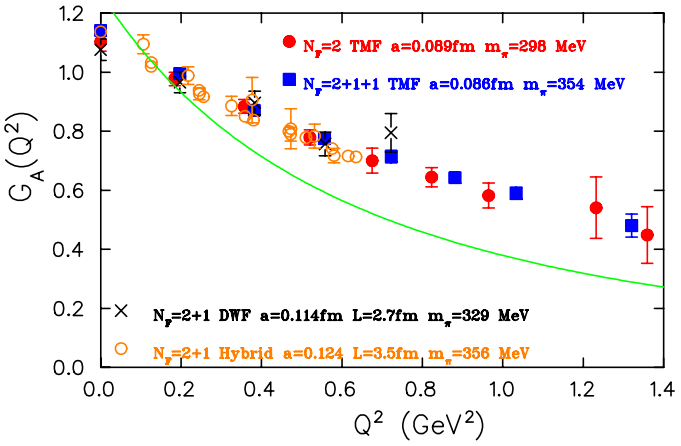

FIG. 12: Q^2-dependence of $G_A(Q^2)$ for N_f=2+1+1 at m_π = 354 MeV (filled blue squares) and the N_f=2 [3] at m_π = 298 MeV (filled red circles) twisted mass data on a lattice with spatial length L = 2.8 fm and similar lattice spacing. We also show results with N_f=2+1 DWF at m_π = 329 MeV, L = 2.7 fm (crosses) [5] and with a hybrid action with N_f=2+1 staggered sea and DWF at m_π = 356 MeV and L = 3.5 fm (open orange circles) [45].

We next discuss the results obtained for the isovector electromagnetic form factors, $G_E(Q^2)$ and $G_M(Q^2)$. In Fig. 14 we compare our N_f=2+1+1 results as the pion mass decreases from 354 MeV to 210 MeV. As can be seen, the values for both quantities decrease towards the experimental values shown by the solid line, which is J. Kelly's parameterization to the experimental data [51]. In particular, for $G_M(Q^2)$ lattice results

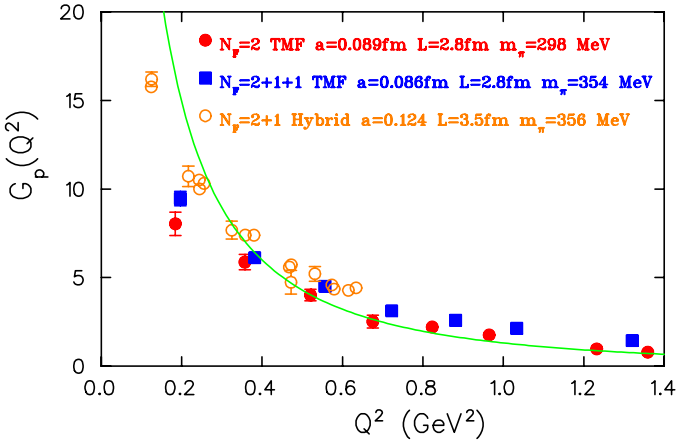

FIG. 13: The Q^2-dependence of $G_p(Q^2)$. The notation is the same as that in Fig. 12.

at $m_\pi = 210$ MeV become consistent with the experimental results. In order to extract the value of $G_M(0)$, we need to extrapolate lattice results at finite Q^2. We parameterized both form factors by a dipole form

$$G_E(Q^2) = \frac{1}{(1+Q^2/m_E^2)^2}\,,$$
$$G_M(Q^2) = \frac{G_M(0)}{(1+Q^2/m_M^2)^2}\,. \qquad (24)$$

The values of $G_M(0)$ extracted are shown in Fig. 14, as well as, the resulting fits with the dashed lines. The overall trend of the lattice QCD data clearly shows that as the pion mass decreases they approach the experimental values. However, even at $m_\pi = 210$ MeV the value of $G_M(0)$, which determines the isovector anomalous magnetic moment, is still underestimated. In Table IV we tabulate the resulting fit parameters m_E, $G_M(0)$ and m_M for the two N_f=2+1+1 ensembles extracted from the dipole fits of Eqs. (24).

β	m_E (GeV)	$G_M(0)$	m_M (GeV)
1.95	1.17(32)	3.93(12)	1.30(08)
2.10	0.86(07)	3.86(34)	0.99(15)

TABLE IV: Results on the nucleon electric and magnetic mass extracted by fitting to the dipole form of Eq. (24).

In Fig. 15 we show the Q^2 dependence of $G_E(Q^2)$ and $G_M(Q^2)$ at $\beta = 2.10$ and $m_\pi = 210$ MeV comparing it to the smallest available pion mass of 262 MeV obtained using N_f=2 ensembles. Once again we do not observe any sizable effects due to the strange and charm quarks in the sea.

It is useful to compare TMF results to those obtained within different fermion discretization schemes. In particular, we compare in Figs. 16 and 17with results obtained using N_f=2+1 DWF [4], N_f=2 Wilson improved clover fermions [48] and using the hybrid action [45] for a pion mass of about 300 MeV. We see a nice agreement among all lattice results for $G_E(Q^2)$, confirming that cut-off effects are small for these actions. In the case of $G_M(Q^2)$ there is also an overall agreement except in the case of the N_f=2 clover results. These results are somewhat lower and are more in agreement with our results at $m_\pi = 210$ MeV. The reason for this is unclear and might be due to limited statistics as these data carry the largest errors.

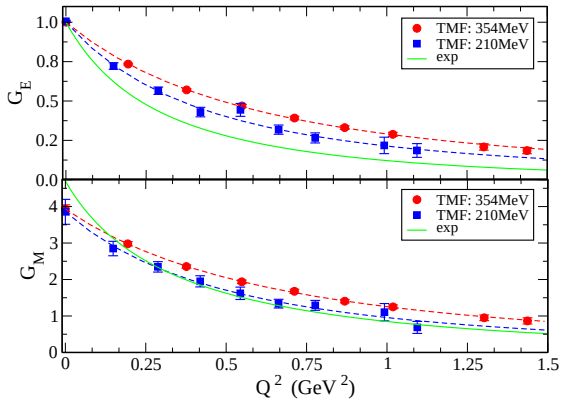

FIG. 14: Comparison of the N_f=2+1+1 twisted mass data on $G_E(Q^2)$ (upper) and $G_M(Q^2)$ (lower) for the two different pion masses considered. The solid lines are Kelly's parameterization of the experimental data [51], whereas the dashed lines are dipole fits to the lattice QCD data.

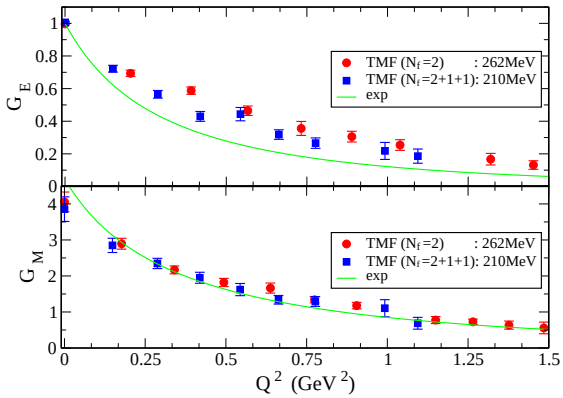

FIG. 15: The Q^2-dependence of $G_E(Q^2)$ (upper) and $G_M(Q^2)$ (lower) for N_f=2+1+1 TMF at $m_\pi = 210$ MeV (filled blue squares) and N_f=2 TMF at $m_\pi = 262$ MeV (filled red circles).

Having fitted the electromagnetic form factors we can extract the isovector anomalous magnetic moment and root mean square (r.m.s.) radii. The anomalous magnetic moment is given by the Pauli form factor $F_2(0)$ and the slope of F_1 at $Q^2 = 0$ determines the transverse size of the hadron, $\langle r_\perp^2 \rangle = -4dF_1/dQ^2|_{Q^2=0}$. In the non-relativistic limit the r.m.s. radius is related to the slope of the form factor at zero momentum transfer. Therefore the r.m.s. radii can be obtained from the values of the

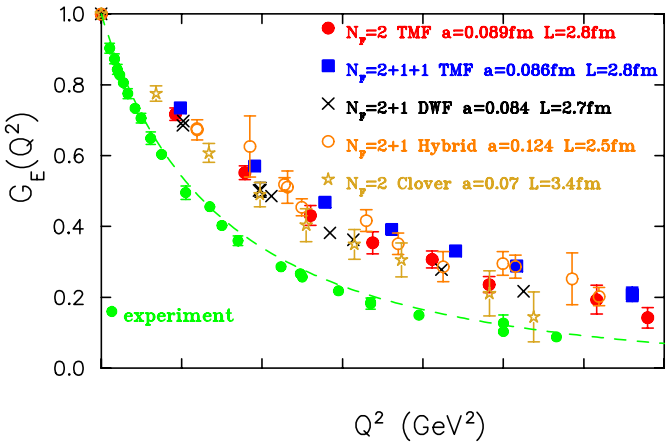

FIG. 16: The Q^2-dependence of $G_E(Q^2)$. We show results for N_f=2+1+1 at m_π = 354 MeV (filled blue squares) and N_f=2 [1] at m_π = 298 MeV (filled red circles) TMF data on a lattice with spatial length L = 2.8 fm and similar lattice spacing. We also show results with N_f=2+1 DWF at m_π = 297 MeV, L = 2.7 fm (crosses) [4], with a hybrid action with N_f=2+1 staggered sea and DWF at m_π = 293 MeV and L = 2.5 fm (open orange circles) [45], and N_f=2 clover at m_π = 290 MeV and L = 3.4 fm (asterisks) [48]. The solid line is Kelly's parameterization of the experimental data [51] from a number of experiments as given in Ref. [51].

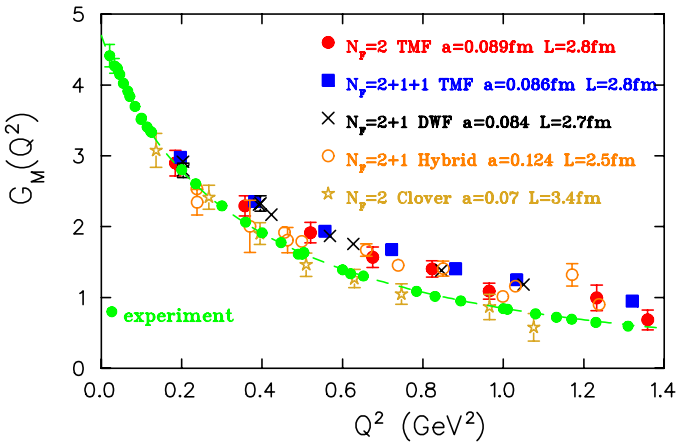

FIG. 17: The Q^2-dependence of $G_M(Q^2)$. The notation is the same as that in Fig. 16.

dipole masses by using

$$\langle r_i^2 \rangle = -\frac{6}{F_i(Q^2)} \frac{dF_i(Q^2)}{dQ^2}|_{Q^2=0} = \frac{12}{m_i^2}, \qquad i = 1, 2 \quad . \tag{25}$$

The electric and magnetic radii are given by $\langle r^2_{E,M} \rangle = 12/m^2_{E,M}$ and can be directly evaluated from the values of the parameters listed in Table IV. In Fig. 18 we present our results on the anomalous magnetic moment, Dirac and Pauli r.m.s. radii. As can be seen, the new results at m_π = 210 MeV, although they are still lower than the experimental value, show an increase towards that value. In Ref. [7] an analysis of the results using the summation

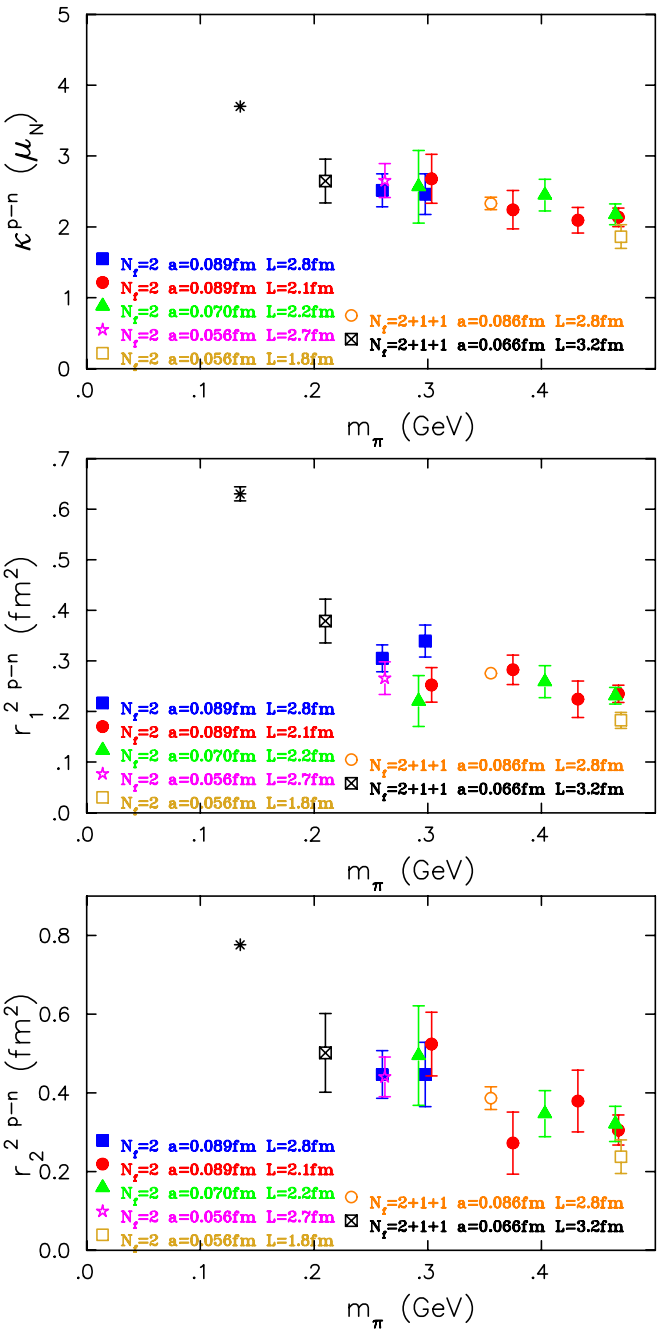

FIG. 18: Twisted mass fermion results with N_f=2 [3] and with N_f=2+1+1, for the isovector anomalous magnetic moment, κ^{p-n} in Bohr magnetons (upper), Dirac r.m.s. radius (middle) and Pauli r.m.s. radius (lower) panel. The notation is the same as that in Fig. 6.

method at m_π = 147 MeV with N_f=2+1 clover fermions was carried out. It was shown that the value of these three quantities increases to bring agreement with the experimental value. This is an encouraging result that needs to be confirmed.

B. Nucleon generalized form factors with one derivative operators

In this section we present results on the nucleon matrix elements of the isovector one-derivative operators defined in Eq. (22). Like g_A, $A_{20}(Q^2{=}0)$ and $\tilde{A}_{20}(Q^2{=}0)$ can be extracted directly from the corresponding matrix element at $Q^2 = 0$. On the other hand, $B_{20}(Q^2{=}0)$, $C_{20}(Q^2{=}0)$ and $\tilde{B}_{20}(Q^2{=}0)$, like G_M and G_p, can not be extracted at $Q^2 = 0$. Therefore one needs to extrapolate lattice data at $Q^2{\neq}0$ by performing a fit.

In Fig. 19 we compare our lattice data of the unpolarized and polarized isovector moments obtained for $N_f{=}2$ [1] TMF for different lattice spacings and volumes to the $N_f{=}2{+}1{+}1$ TMF results of this work. As can be seen, there are no detectable cut-off effects for the lattice spacings considered here, nor volume dependence at least for pion masses up to about 300 MeV where different volumes were analyzed. Also, there is consistency among results obtained using $N_f{=}2$ and $N_f{=}2{+}1{+}1$ gauge configurations indicating that strange and charm quark effects are small. We would like to point out that the renormalization constant for the vector one-derivative operator is larger by about 2% than the one used in Ref. [34] since in converting to $\overline{\rm MS}$ we used the 2-loop conversion factor instead of the 3-loop result, thus increasing the value of $\langle x\rangle_{u-d}$. As in the case of the nucleon axial charge, a number of studies were undertaken to examine the role of excited states in the extraction of $\langle x\rangle_{u-d}$. A high statistics analysis carried out with twisted mass fermions at $m_\pi = 354$ MeV has shown that excited state contamination accounted for a decrease of about 10% in the value of $\langle x\rangle_{u-d}$ as compared to the value extracted using sink-source separation of about 1 fm [33, 34]. The most noticeable behavior regarding these TMF results is that the values obtained at $m_\pi = 210$ MeV for both $\langle x\rangle_{u-d}$ and $\langle x\rangle_{\Delta u-\Delta d}$ approach the physical value. We would like to remark that the phenomenological value of $\langle x\rangle_{u-d}$ extracted from different analysis [52–57] shows a spread, which, however, is significantly smaller than the discrepancy as compared to the deviation shown by lattice data for pion masses higher than the physical point. The same applies for $\langle x\rangle_{\Delta u-\Delta d}$ [58, 59].

Recent results on A_{20} and $\tilde{A}_{20}$ from a number of groups using different discretization schemes are shown in Fig. 20. We limit ourselves to results extracted from fitting to the ratio given in Eq. (17) taking a source-sink separation of 1 fm to 1.2 fm. Once more, there is an overall agreement among these lattice data indicating that cut-off effects are small for lattice spacings $\lesssim$ 0.1fm, for the improved actions used. The decrease seen using TMF at $m_\pi = 210$ MeV is corroborated by other recent results at near physical pion masses: for $\langle x\rangle_{u-d}$ results from Ref. [6] using clover-improved fermions at $m_\pi = 157$ MeV and $Lm_\pi = 2.74$, as well as, from Ref. [47] using $N_f{=}2{+}1$ flavors of tree-level clover-improved Wilson fermions coupled to double HEX-smeared gauge fields at $m_\pi = 149$ MeV and $Lm_\pi = 4.2$,

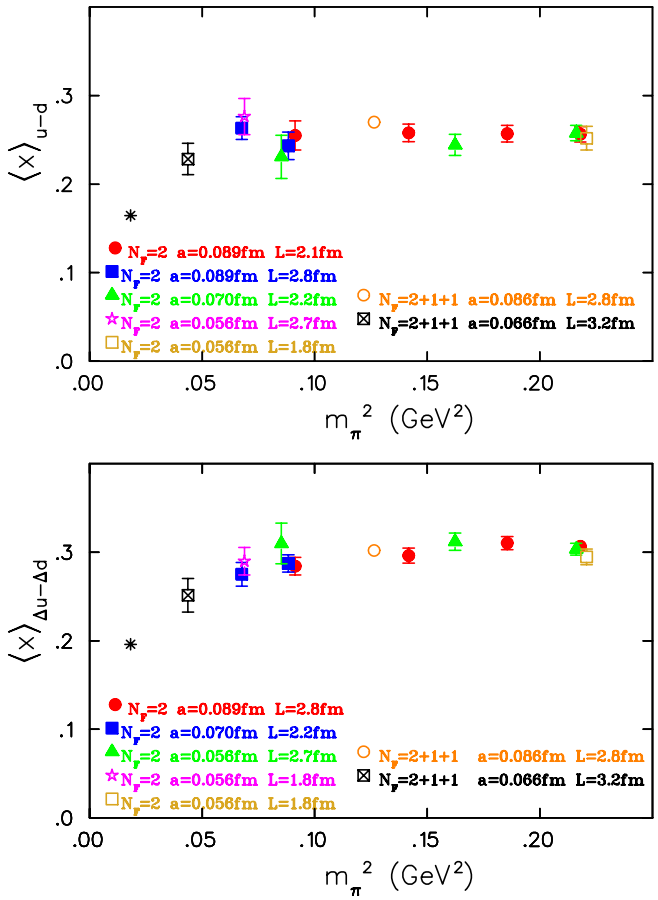

FIG. 19: Results for $\langle x\rangle_{u-d}$ (upper) and $\langle x\rangle_{\Delta u-\Delta d}$ (lower) using $N_f{=}2$ and $N_f{=}2{+}1{+}1$ twisted mass fermions as a function of the pion mass. We show results for (i) $N_f{=}2$ twisted mass fermions with $a = 0.089$ fm (filled red circles for $L = 2.1$ fm and filled blue squares for $L = 2.8$ fm), $a = 0.070$ fm (filled green triangles), and $a = 0.056$ fm (open stars for $L = 2.7$ fm and open square for $L = 1.8$ fm); (ii) $N_f{=}2{+}1{+}1$ twisted mass fermions with $a = 0.0863$ fm (open circle) and $a = 0.0657$ fm (square with a cross). The physical point, shown by the asterisk, is from Ref. [55] for the unpolarized and from Ref. [58, 59] for the polarized first moment.

also decrease towards the physical value. Furthermore, for the latter case, three sink-source separations up to 1.4 fm were utilized to apply the summation method reducing the value shown in Fig. 20 further to bring it into agreement with the experimental one [7]. Note that this is opposite to what was found for g_A where its value decreased further away from the experimental value. The agreement between the values found in Refs. [6] and [47], despite the different volumes, indicates that the volume dependence of this quantity is small, again different from what was claimed in Ref. [46] for g_A. In Ref. [47] it was demonstrated that contributions from excited states increase as the pion mass decreases towards its physical value indicating that excited state contamination may explain the discrepancy between lattice results and the experimental value. Further studies of excited state con-

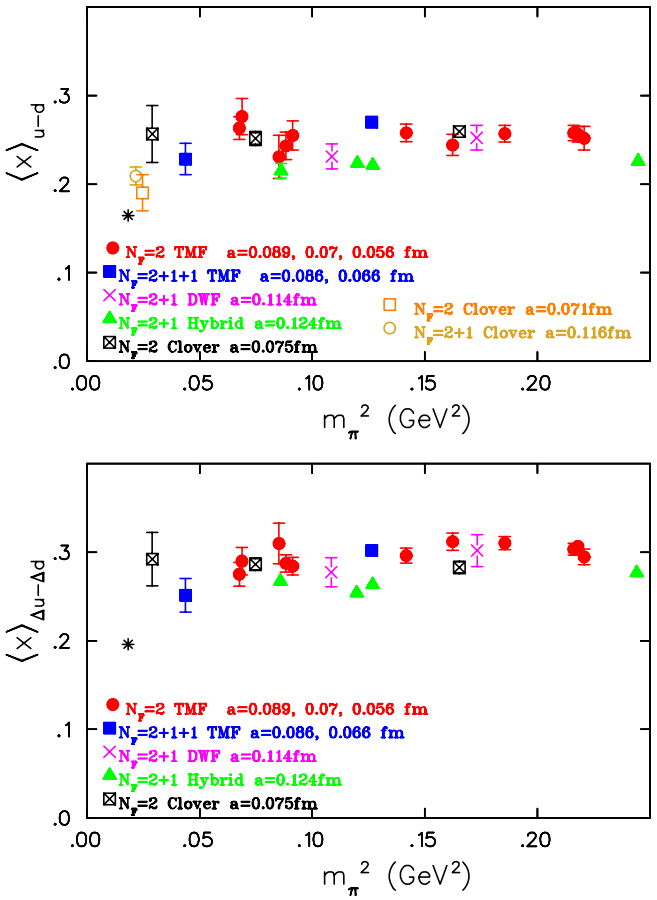

FIG. 20: Results for $\langle x \rangle_{u-d}$ (upper) and $\langle x \rangle_{\Delta u-\Delta d}$ (lower) obtained in this work are shown with the red filled circles for N_f=2 and with the blue filled squares for N_f=2+1+1. We compare with (i) N_f=2+1 DWF for $a = 0.114$ fm [60]; (ii) N_f=2+1 using DWF for the valence quarks on staggered sea [45] with $a = 0.124$ fm; (iii) N_f=2 clover with $a = 0.075$ fm [61]. For $\langle x \rangle_{u-d}$ we also show recent results using N_f=2 clover with $a = 0.071$ fm [6] and N_f=2+1 of tree-level clover-improved Wilson fermions coupled to double HEX-smeared gauge fields with $a = 0.116$ fm [7].

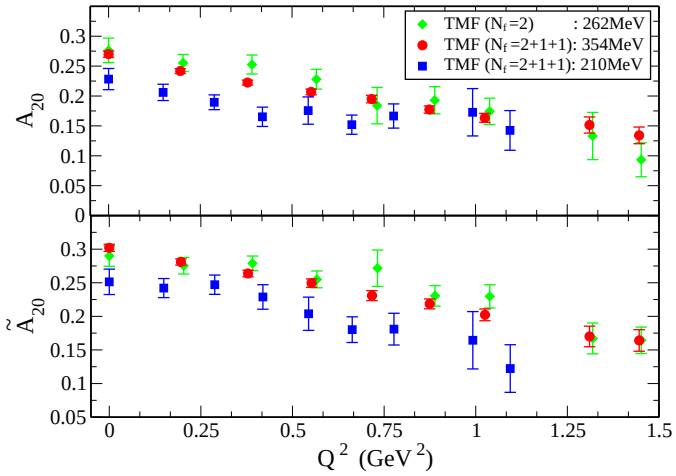

FIG. 21: The Q^2-dependence of $A_{20}(Q^2)$ (upper) and $\tilde{A}_{20}(Q^2)$ (lower) for N_f=2 with $a = 0.056$ fm and $m_\pi = 262$ MeV (filled green diamonds), and N_f=2+1+1 with i) $a = 0.066$ fm and $m_\pi = 210$ MeV (filled blue squares); ii) $a = 0.086$ fm and $m_\pi = 354$ MeV (filled red circles).

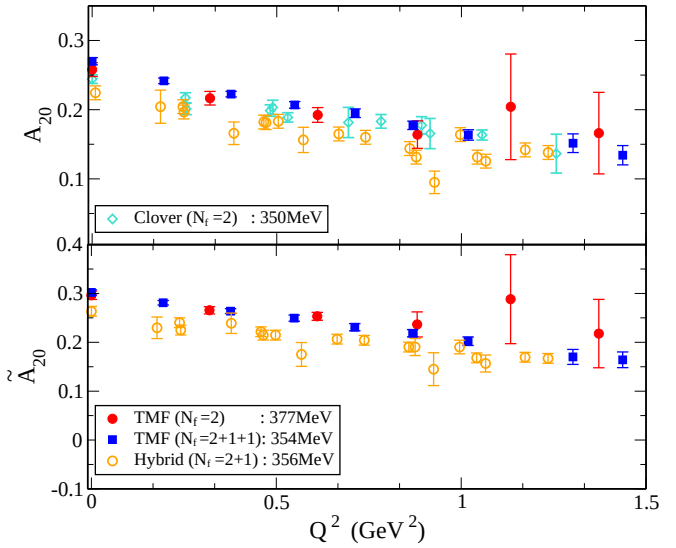

FIG. 22: The Q^2-dependence of $A_{20}(Q^2)$ (upper) and $\tilde{A}_{20}(Q^2)$ (lower) shown for i) N_f=2 twisted mass fermions for $a = 0.089$ fm, $m_\pi = 377$ MeV (filled red circles) [1]; ii) N_f=2+1+1 twisted mass fermions (this work) for $a = 0.086$ fm and $m_\pi = 354$ MeV; iii) N_f=2 clover fermions for $a \sim 0.08$ fm and $m_\pi \sim 350$ MeV (open cyan diamonds) [62]; and iv) N_f=2+1 with DWF valence on a staggered sea for $a = 0.124$ fm and $m_\pi = 356$ MeV (open orange circles) [45].

tamination at near physical pion mass will be essential in order to establish this conclusion.

The Q^2-dependence of $A_{20}(Q^2)$ and $\tilde{A}_{20}(Q^2)$ is shown in Fig. 21 for our two N_f=2+1+1 ensembles and for the N_f=2 ensemble with the smallest available mass, namely 262 MeV. Since strange and charm quark effects have been shown to be small, one can study the dependence on the pion mass by comparing with results obtained using N_f=2 TMF. As the pion mass decreases from 354 MeV to 262 MeV there is no significant change in the values of $A_{20}(Q^2)$ and $\tilde{A}_{20}(Q^2)$ over the whole Q^2 range. Reducing the pion mass further to 210 MeV leads to a larger decrease in the values of both $A_{20}(Q^2)$ and $\tilde{A}_{20}(Q^2)$ indicating that near the physical regime the pion mass dependence becomes stronger. Such a pion mass dependence is what one would expect if the lattice QCD data at $Q^2 = 0$ are to agree with the experimental value. In Fig. 22 we compare our results using TMF to hybrid results and, for $A_{20}(Q^2)$, we also include N_f=2 clover at similar pion masses. There is an overall agreement between clover and TMF for $A_{20}(Q^2)$, whereas the hybrid data are somewhat lower. The fact that they are renormalized perturbatively might explain their lower values.

Before closing this section we present in Fig. 23 results

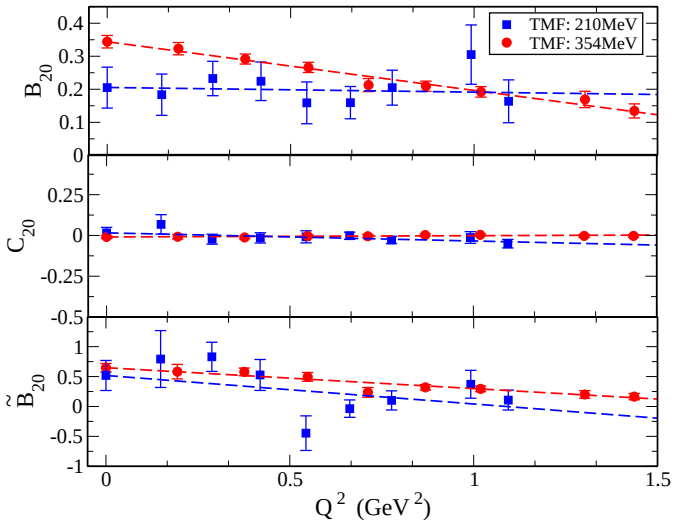

FIG. 23: The Q^2-dependence of $B_{20}(Q^2)$, $C_{20}(Q^2)$ and $\tilde{B}_{20}(Q^2)$ for N_f=2+1+1 computed at $\beta = 1.95$ ($m_\pi = 354$ MeV) and $\beta = 2.10$ ($m_\pi = 210$) MeV. The dashed lines show the linear fits to $B_{20}(Q^2)$, $C_{20}(Q^2)$ and $\tilde{B}_{20}(Q^2)$ to extract the value at $Q^2 = 0$ shown here.

for $B_{20}(Q^2)$, $C_{20}(Q^2)$, $\tilde{B}_{20}(Q^2)$ for the two N_f=2+1+1 ensembles. All these three GFFs can not be extracted at Q^2=0 directly from the matrix element and therefore we must extrapolate them using an Ansatz to fit the Q^2-dependence. We performed two types of fits: a linear and a dipole fit. Note that for small Q^2 the two are equivalent. It was generally found that a linear fit describes well the data with smaller errors on the fit parameters. We therefore use the fitted values extracted from the linear fit summarized in Table V. $C_{20}(Q^2)$ is consistent with zero for all values of Q^2.

β	$B_{20}(0)$ (GeV)	$C_{20}(0)$	$\tilde{B}_{20}(0)$
1.95	0.344(19)	-0.009(09)	0.648(71)
2.10	0.205(62)	0.016(34)	0.518(251)

TABLE V: Results on $B_{20}(Q^2 = 0)$, $C_{20}(Q^2 = 0)$ and $\tilde{B}_{20}(Q^2 = 0)$ by fitting to a linear Q^2-dependence.

IV. PROTON SPIN

How much of the proton spin is carried by the quarks is a question that is under study ever since the results of the European Muon Collaboration (EMC) claimed that the quarks carried only a small fraction of the proton spin [63]. This became known as the "proton spin crisis". It was proposed that gluons in a polarized proton would carry a fraction of the spin, which however would be unnaturally large if it were to resolve the EMC spin crisis. It is now understood that the resolution of this puzzle requires to take into account the non-perturbative structure of the proton [64]. In order to use our lattice results to obtain information on the spin content of the nucleon we need to evaluate, besides the isovector moments, the isoscalar moments A_{20}^{u+d} and B_{20}^{u+d} since the total angular momentum of a quark in the nucleon is given by

$$J^q = \frac{1}{2}\left(A_{20}^q(0) + B_{20}^q(0)\right) . \tag{26}$$

As already discussed, the total angular momentum J^q can be further decomposed into its orbital angular momentum L^q and its spin component $\Delta\Sigma^q$ as

$$J^q = \frac{1}{2}\Delta\Sigma^q + L^q . \tag{27}$$

The spin carried by the u- and d- quarks is determined using $\Delta\Sigma^{u+d} = \tilde{A}_{10}^{u+d}$, and therefore we need the isoscalar axial charge. The isoscalar quantities take contributions from the disconnected diagram, which are notoriously difficult to calculate and are neglected in most current evaluations of GFFs. These contributions are currently being computed using improved stochastic techniques [65, 66]. Under the assumption that these are small we may extract information on the fraction of the nucleon spin carried by quarks.

In Fig. 24 we show our results for the isoscalar $G_A(Q^2)^{u+d}$, $A_{20}(Q^2)^{u+d}$, $B_{20}(Q^2)^{u+d}$ and $C_{20}(Q^2)^{u+d}$ for the two N_f=2+1+1 ensembles analyzed in this work. It was shown using the N_f=2 ensembles at three lattice spacings smaller than 0.1 fm [1] that cut-off effects are small. We expect a similar behaviour for our N_f=2+1+1 ensembles. Therefore, we perform a chiral extrapolation using directly all our lattice data for the N_f=2 and N_f=2+1+1 ensembles. Having both isoscalar and isovector quantities we can extract the angular momentum J^u and J^d carried by the u- and d- quarks. In order to extract these quantities we need to know the value of B_{20} at $Q^2 = 0$. As explained already, one has to extrapolate the lattice results using an Ansatz for the Q^2-dependence to extract B_{20} at $Q^2 = 0$ and two ansätze were considered for the Q^2-dependence, a dipole and a linear form. For the linear fit we use two fitting ranges one up to $Q^2 = 0.25$ GeV^2 and the other up to $Q^2 = 4$ GeV^2. Thus the extrapolation introduces model dependence in the extraction of the quark spin J^q. The values of B_{20} extracted using these three ansätze are consistent, with the dipole fit resulting in parameters that carry large errors. In extracting the angular momentum we thus use the data extracted using the extended range linear fit and given in Table V.

We first compare in Fig. 25 our results for the u- and d- quark angular momentum J^q, spin $\Delta\Sigma^q$ and orbital angular momentum L^q to those obtained using the hybrid action of Ref. [45]. As can be seen, the lattice data are in agreement within our statistical errors indicating that lattice artifacts are smaller than the current statistical errors, also for these quantities. In order to get an approximate value for these observables at the physical point we perform a chiral extrapolation using heavy

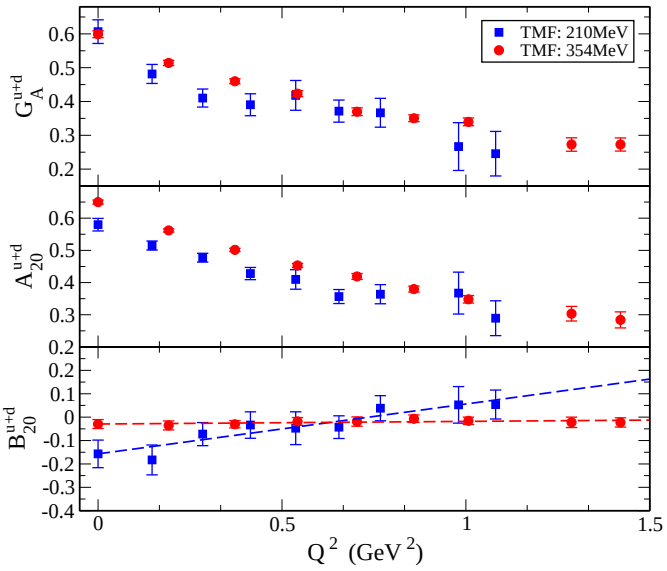

FIG. 24: The Q^2-dependence of the isoscalar $G_A(Q^2)$, $A_{20}(Q^2)$ and $B_{20}(Q^2)$ for N_f=2+1+1 computed at $\beta = 1.95$ ($m_\pi = 354$ MeV) and $\beta = 2.10$ ($m_\pi = 210$) MeV.

baryon chiral perturbation theory (HBχPT). Combining the expressions for A_{20} and B_{20} [68, 69] in the isoscalar and isovector cases we obtain the following form for the angular momentum

$$J^q = a_0^q \frac{m_\pi^2}{(4\pi f_\pi)^2} \ln \frac{m_\pi^2}{\lambda^2} + a_1^q m_\pi^2 + a_2^q \,, \qquad (28)$$

and take $\lambda^2 = 1$ GeV^2. We also carry out a chiral fit using $\mathcal{O}(p^2)$ covariant baryon chiral perturbation theory (CBχPT) [70]. All the expressions are collected in Appendix B for completeness. As noted these chiral extrapolations are to give an indicative idea of what one might obtain since their range of validity may require using pion masses closer to the physical point.

In order to correctly estimate the errors both on the data points and on the error bands, we apply an extended version of the standard jackknife error procedure known as superjackknife analysis [45]. This generalized method is applicable for analyzing data computed on several gauge ensembles. This is needed for carrying out the chiral extrapolations for the angular momentum J^q, orbital angular momentum L^q and spin $\Delta\Sigma^q$. Although, there is no correlation among data sets from different gauge ensembles, the data within each ensemble are correlated. This analysis method allows us to consider a different number of lattice QCD measurements for each ensemble taking into account correlations within each ensemble correctly. It should be apparent that the superjackknife reduces to the standard jackknife analysis in the case of a single ensemble.

In Fig. 26 we show the chiral fits for J^q. In the upper panel we show the chiral extrapolation using CBχPT and in the lower the extrapolation using HBχPT. Both have the same qualitative behavior yielding a much smaller

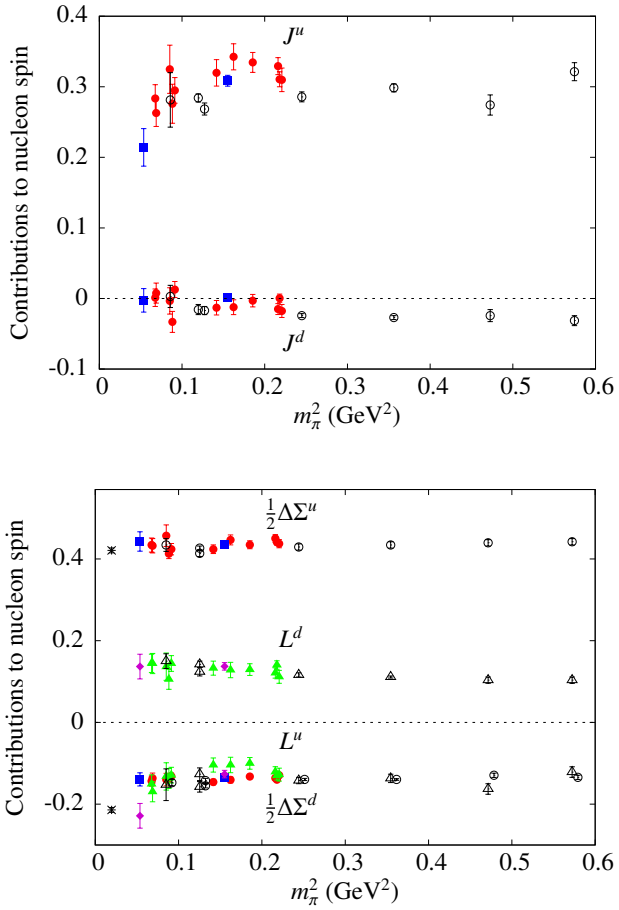

FIG. 25: Comparison of TMF results (filled symbols) to those using a hybrid action [45] (open symbols). The upper panel shows the angular momentum J^u and J^d for u- and d- quarks respectively (blue filled squares for N_f=2+1+1 and filled red circles for N_f=2). The lower panel shows the quark spin (same symbols as for J^q) and the orbital angular momentum (filled green triangles for N_f=2 and filled magenta diamonds for N_f=2+1+1). The errors are determined by carrying out a superjackknife analysis described in Ref. [45]. The experimental value of $\Delta\Sigma^{u,d}$ is shown by the asterisks and are taken from the HERMES 2007 analysis [67].

contribution to the angular momentum from the d-quark than that from the u-quarks. In the plot we also show the band of allowed values if the fit were performed on data that used the $Q^2 = 0$ extrapolated values of B_{20} from the limited range linear fit. As can be seen, the two bands are consistent. Had we used a dipole Ansatz for the $Q^2 = 0$ extrapolation, the error band would also be consistent but much larger, especially for smaller pion masses, where there are no lattice data. Therefore, for the rest of the discussion we only show the extrapolation bands obtained using the limited and full Q^2 range linear fits. These results are in qualitative agreement with the chiral extrapolations using the data obtained with the hybrid action [45].

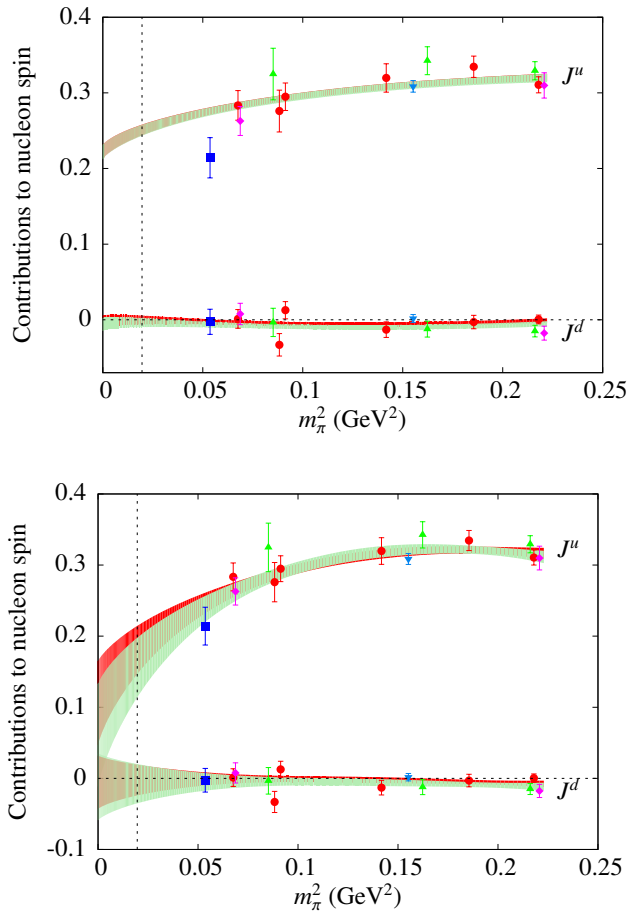

FIG. 26: Chiral extrapolation using CBχPT (upper) and HBχPT (lower) for the angular momentum carried by the u-and d- quarks. The red band is the chiral fit using the data for $B_{20}(Q^2=0)$ obtained by a linear extrapolation of $B_{20}(Q^2)$ using Q^2 values up to $Q^2 = 4$ GeV^2 whereas the green band is the fit using values of $B_{20}(0)$ extracted from a linear extrapolation of $B_{20}(Q^2)$ using Q^2 values up to ~ 0.25 GeV^2. The data shown in the plot are obtained from the extended linear Q^2 extrapolation. Filled red circles are data for N_f=2 at $\beta = 3.9$, filled green triangles for N_f=2 at $\beta = 4.05$, filled magenta diamonds for N_f=2 at $\beta = 4.2$, filled light blue inverted triangle for N_f=2+1+1 at $\beta = 1.95$ and filled blue square for N_f=2+1+1 at $\beta = 2.10$.

In Fig. 27 we show separately the orbital angular momentum and spin carried by the u- and d- quarks. The total orbital angular momentum carried by the quarks tends to small negative values as we approach the physical point. This is a crucial result and it would be important to perform a calculation at lower pion mass to confirm that this trend towards negative values remains [71]. After chiral extrapolation, the value obtained at the physical point is consistent with zero in agreement with the result by LHPC. We summarize the values for the angular momentum, orbital angular momentum and spin in the proton at the physical point in Table VI. The

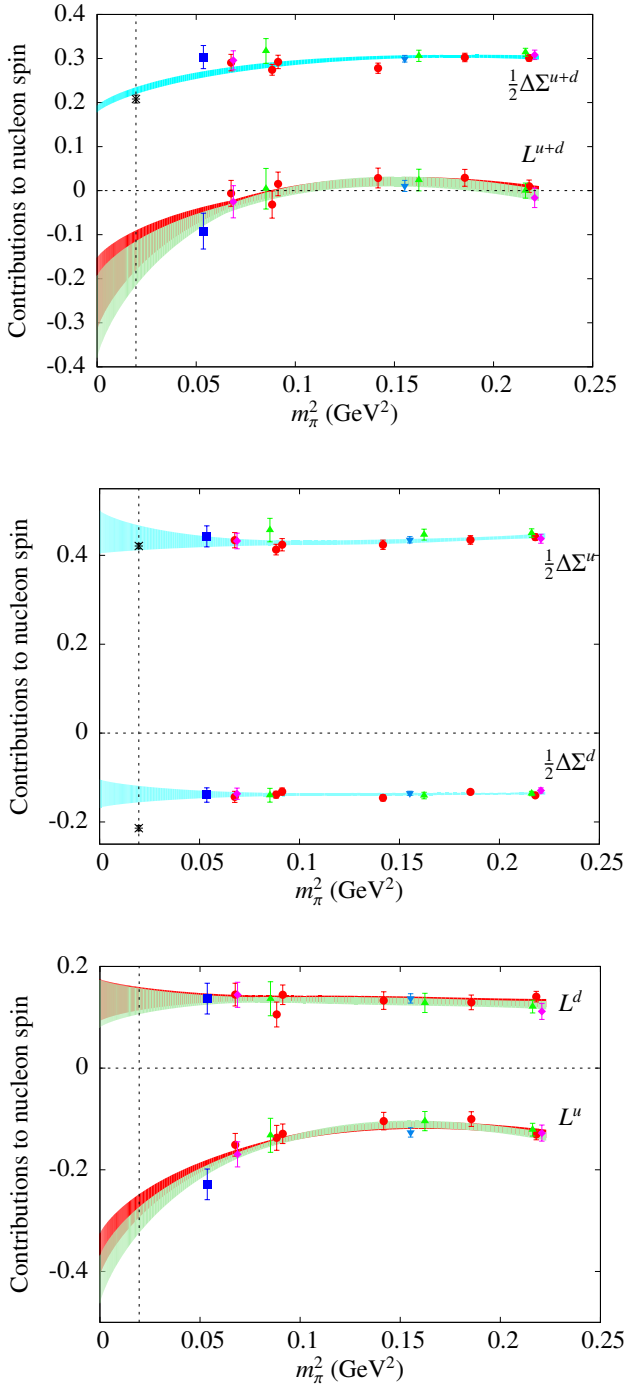

FIG. 27: Chiral extrapolation using HBχPT. The upper graph shows the spin and orbital angular momentum carried by u- and d- quarks, whereas the middle and lower graphs show the spin and orbital angular momentum carried separately by the u- and d- quarks. The errors are determined through a superjacknife analysis. The physical points, shown by the asterisks are from the HERMES 2007 analysis [67]. The notation is the same as that in Fig. 26.

	CBχPT	HBχPT	experiment
J^{u-d}		0.218179(12)	
J^{u+d}		0.168(42)	
J^{u}	0.249616(7)	0.173(35)	
J^{d}	-0.000242(6)	-0.003(17)	
$\Delta\Sigma^{u-d}/2$		0.462(9)	
$\Delta\Sigma^{u+d}/2$		0.225(8)	0.208(9)
$\Delta\Sigma^{u}/2$		0.440(29)	0.421(6)
$\Delta\Sigma^{d}/2$		-0.137(19)	-0.214(6)
L^{u-d}		-0.252(8)	
L^{u+d}		-0.141(48)	
L^{u}		-0.196(23)	
L^{d}		0.055(24)	

TABLE VI: Values of nucleon spin observables at the physical point using CBχPT and HBχPT and from experiment [67].

value obtained for the $\Delta\Sigma^u$ agrees with the experimental value whereas the extrapolated LQCD value of $\Delta\Sigma^d$ is less negative. As already pointed out, results closer to the physical pion mass will be essential to resolve such discrepancies. In addition, the computation of the disconnected diagrams will eliminate a remaining systematic error and will enable us to have final results on the spin carried by the quarks and consequently on the gluon contribution to the nucleon spin.

V. CONCLUSIONS

We have performed an analysis on the generalized form factors $G_E(Q^2)$, $G_M(Q^2)$, $G_A(Q^2)$, $G_p(Q^2)$, $A_{20}(Q^2)$, $B_{20}(Q^2)$, $C_{20}(Q^2)$, $\tilde{A}_{20}(Q^2)$ and $\tilde{B}_{20}(Q^2)$, extracted from the nucleon matrix elements of the local and one-derivative vector and axial-vector operators using N_f=2+1+1 flavors of twisted mass fermions. Our results are non-perturbatively renormalized and they are presented in the $\overline{\rm MS}$ scheme at a scale of 2 GeV. The comparison of the results using N_f=2 and N_f=2+1+1 twisted mass fermions with the results obtained using other discretizations show an overall agreement for pion masses down to about 200 MeV. The compatibility of N_f=2 data with those including a dynamical strange and a charm quark is an indication that any systematic effect of strange and charm sea quark effects on these quantities for which disconnected contributions were neglected is small. The twisted mass fermion results on the axial nucleon charge remain smaller than the experimental value. The recent results using N_f=2 [46] and N_f=2+1 [7] clover-improved fermions near the physical pion mass are somewhat in conflict with each other and hard to interpret in a consistent way. Therefore, further investigation is required to resolve the issue. For the unpolarized isovector momentum fraction lattice results show a decrease as we approach the physical pion mass with indications of excited state contamination that needs further investigation.

We also analyze the corresponding isoscalar quantities using directly our lattice data. Of particular interest here is to extract results that shed light on the spin content of the nucleon. Assuming that the disconnected contributions to the isoscalar quantities are small we can extract the spin carried by the quarks in the nucleon. For the chiral extrapolations of these quantities we use HBχPT and CBχPT theory applied to all our N_f=2 and N_f=2+1+1 data. We find that the spin carried by the d-quark is almost zero whereas the u-quarks carry about 50% of the nucleon spin. This result is consistent with other lattice calculations [45].

Acknowledgments

We would like to thank all members of ETMC for a very constructive and enjoyable collaboration and for the many fruitful discussions that took place during the development of this work.

Numerical calculations have used HPC resources from John von Neumann-Institute for Computing on the Jugene systems at the research center in Jülich through the PRACE allocation, 3rd regular call. It also used the Cy-Tera facility of the Cyprus Institute under the project Cy-Tera (NEA ΥΠΟΔΟΜΗ/ΣΤΡΑΤΗ/0308/31), first access call (project lspro113s1). We thank the staff members for their kind and sustained support. This work is supported in part by the Cyprus Research Promotion Foundation under contracts ΚΥ-Γ/0310/02/ and TECHNOLOGY/ΘΕΠΙΣ/0311(BE)/16, and the Research Executive Agency of the European Union under Grant Agreement number PITN-GA-2009-238353 (ITN STRONGnet). This work is also supported in part by the DFG Sonderforschungsbereich/Transregio SFB/TR9. K. J. was supported in part by the Cyprus Research Promotion Foundation under contract ΠΡΟΣΕΛΚΥΣΗ/ΕΜΠΕΙΡΟΣ/0311/16.

[1] C. Alexandrou, J. Carbonell, M. Constantinou, P. Harraud, P. Guichon, et al., Phys.Rev. **D83**, 114513 (2011), 1104.1600.

[2] C. Alexandrou, M. Brinet, J. Carbonell, M. Constantinou, P. Harraud, et al., Phys.Rev. **D83**, 094502 (2011), 1102.2208.

[3] C. Alexandrou et al. (ETM Collaboration), Phys.Rev. **D83**, 045010 (2011), 1012.0857.

[4] S. N. Syritsyn et al., Phys. Rev. **D81**, 034507 (2010), 0907.4194.

[5] T. Yamazaki et al., Phys. Rev. **D79**, 114505 (2009), 0904.2039.

[6] G. S. Bali, S. Collins, M. Deka, B. Glassle, M. Gockeler, et al., Phys.Rev. **D86**, 054504 (2012), 1207.1110.

[7] J. Green, M. Engelhardt, S. Krieg, J. Negele, A. Pochinsky, et al. (2012), 1209.1687.

[8] A. Sternbeck, M. Gockeler, P. Hagler, R. Horsley, Y. Nakamura, et al., PoS **LATTICE2011**, 177 (2011), 1203.6579.

[9] S. Collins, M. Gockeler, P. Hagler, R. Horsley, Y. Nakamura, et al., Phys.Rev. **D84**, 074507 (2011), 1106.3580.

[10] D. Brommel et al. (QCDSF-UKQCD), PoS **LAT2007**, 158 (2007), 0710.1534.

[11] P. Hagler et al. (LHPC), Phys. Rev. **D77**, 094502 (2008), 0705.4295.

[12] D. Mueller, D. Robaschik, B. Geyer, F. Dittes, and J. Horejsi, Fortsch.Phys. **42**, 101 (1994), hep-ph/9812448.

[13] X.-D. Ji, Phys.Rev. **D55**, 7114 (1997), hep-ph/9609381.

[14] A. Radyushkin, Phys.Rev. **D56**, 5524 (1997), hep-ph/9704207.

[15] X.-D. Ji, Phys.Rev.Lett. **78**, 610 (1997), hep-ph/9603249.

[16] A. Airapetian et al. (HERMES collaboration), JHEP **0911**, 083 (2009), 0909.3587.

[17] S. Chekanov et al. (ZEUS Collaboration), JHEP **0905**, 108 (2009), 0812.2517.

[18] F. Aaron et al. (H1 Collaboration), Phys.Lett. **B659**, 796 (2008), 0709.4114.

[19] C. M. Camacho et al. (Jefferson Lab Hall A Collaboration, Hall A DVCS Collaboration), Phys.Rev.Lett. **97**, 262002 (2006), nucl-ex/0607029.

[20] S. Stepanyan et al. (CLAS Collaboration), Phys.Rev.Lett. **87**, 182002 (2001), hep-ex/0107043.

[21] J. Beringer et al. (Particle Data Group), Phys.Rev. **D86**, 010001 (2012).

[22] C. Alexandrou, V. Drach, K. Hadjiyiannakou, K. Jansen, G. Koutsou, et al., PoS **LATTICE2012**, 184 (2012), 1211.0126.

[23] R. Frezzotti, P. A. Grassi, S. Sint, and P. Weisz (Alpha), JHEP **0108**, 058 (2001), hep-lat/0101001.

[24] P. Weisz, Nucl. Phys. **B212**, 1 (1983).

[25] R. Frezzotti and G. Rossi, JHEP **0408**, 007 (2004), hep-lat/0306014.

[26] R. Baron, P. Boucaud, J. Carbonell, A. Deuzeman, V. Drach, et al., JHEP **1006**, 111 (2010), 1004.5284.

[27] C. Alexandrou, S. Gusken, F. Jegerlehner, K. Schilling, and R. Sommer, Nucl. Phys. **B414**, 815 (1994), hep-lat/9211042.

[28] S. Gusken, Nucl. Phys. Proc. Suppl. **17**, 361 (1990).

[29] C. Alexandrou et al. (European Twisted Mass), Phys. Rev. **D78**, 014509 (2008), 0803.3190.

[30] D. Dolgov et al. (LHPC), Phys. Rev. **D66**, 034506 (2002), hep-lat/0201021.

[31] C. Alexandrou, S. Dinter, V. Drach, K. Hadjiyiannakou, K. Jansen, et al. (2013), 1302.2608.

[32] M. Gockeler et al., Phys. Rev. **D54**, 5705 (1996), hep-lat/9602029.

[33] C. Alexandrou, M. Constantinou, S. Dinter, V. Drach, K. Jansen, et al., PoS **LATTICE2011**, 150 (2011), 1112.2931.

[34] S. Dinter, C. Alexandrou, M. Constantinou, V. Drach, K. Jansen, et al., Phys.Lett. **B704**, 89 (2011), 1108.1076.

[35] R. Baron et al. (ETM Collaboration), **06**, 111 (2010), arXiv:0410. [hep-lat].

[36] R. Baron et al. (ETM Collaboration), PoS **LATTICE2010**, 123 (2010), 1101.0518.

[37] R. Baron et al. (European Twisted Mass Collaboration), Comput.Phys.Commun. **182**, 299 (2011), 1005.2042.

[38] C. Alexandrou, M. Constantinou, T. Korzec, H. Panagopoulos, and F. Stylianou, Phys.Rev. **D83**, 014503 (2011), 1006.1920.

[39] M. Gockeler et al., Nucl. Phys. **B544**, 699 (1999), hep-lat/9807044.

[40] P. Dimopoulos, R. Frezzotti, G. Herdoiza, K. Jansen, V. Lubicz, et al., PoS **LATTICE2010**, 235 (2010), 1101.1877.

[41] M. Constantinou, V. Lubicz, H. Panagopoulos, and F. Stylianou, JHEP **10**, 064 (2009), 0907.0381.

[42] C. Alexandrou, M. Constantinou, T. Korzec, H. Panagopoulos, and F. Stylianou, Phys.Rev. **D86**, 014505 (2012), 1201.5025.

[43] J. Gracey, Nucl. Phys. **B662**, 247 (2003), [hep-ph/0304113].

[44] S. Capitani, M. Della Morte, G. von Hippel, B. Jager, A. Juttner, et al., Phys.Rev. **D86**, 074502 (2012), 1205.0180.

[45] J. D. Bratt et al. (LHPC) (2010), 1001.3620.

[46] R. Horsley, Y. Nakamura, A. Nobile, P. Rakow, G. Schierholz, et al. (2013), 1302.2233.

[47] J. Green, M. Engelhardt, S. Krieg, J. Negele, A. Pochinsky, et al., PoS **LATTICE2012**, 170 (2012), 1211.0253.

[48] S. Capitani, B. Knippschild, M. Della Morte, and H. Wittig, PoS **LATTICE2010**, 147 (2010), 1011.1358.

[49] J. Green, J. Negele, A. Pochinsky, S. Krieg, and S. Syritsyn, PoS **LATTICE2011**, 157 (2011), 1111.0255.

[50] V. Bernard, L. Elouadrhiri, and U. G. Meissner, J. Phys. **G28**, R1 (2002), hep-ph/0107088.

[51] J. Kelly, Phys. Rev. **C70**, 068202 (2004).

[52] J. Blumlein, H. Bottcher, and A. Guffanti, Nucl.Phys.Proc.Suppl. **135**, 152 (2004), hep-ph/0407089.

[53] J. Blumlein, H. Bottcher, and A. Guffanti, Nucl.Phys. **B774**, 182 (2007), hep-ph/0607200.

[54] S. Alekhin, K. Melnikov, and F. Petriello, Phys.Rev. **D74**, 054033 (2006), hep-ph/0606237.

[55] S. Alekhin, J. Blumlein, S. Klein, and S. Moch, Phys.Rev. **D81**, 014032 (2010), 0908.2766.

[56] P. Jimenez-Delgado and E. Reya, Phys.Rev. **D79**, 074023 (2009), 0810.4274.

[57] A. Martin, W. Stirling, R. Thorne, and G. Watt, Eur.Phys.J. **C64**, 653 (2009), 0905.3531.

[58] A. Airapetian et al. (HERMES Collaboration), Phys.Lett. **B682**, 345 (2010), 0907.2596.

[59] J. Blumlein and H. Bottcher, Nucl.Phys. **B841**, 205 (2010), 1005.3113.

[60] Y. Aoki et al., Phys. Rev. **D82**, 014501 (2010), 1003.3387.

[61] D. Pleiter et al. (QCDSF/UKQCD Collaboration), PoS **LATTICE2010**, 153 (2010), 1101.2326.

[62] D. Brommel, M. Gockeler, P. Hagler, R. Horsley, Y. Nakamura, et al., Eur.Phys.J.ST **162**, 63 (2008), 0804.4706.

[63] J. Ashman et al. (European Muon Collaboration), Phys.Lett. **B206**, 364 (1988).

[64] A. W. Thomas, Int.J.Mod.Phys. **E18**, 1116 (2009), 0904.1735.

[65] C. Alexandrou, M. Constantinou, S. Dinter, V. Drach, K. Hadjiyiannakou, et al., PoS **LATTICE2012**, 163

(2012), 1211.4447.
[66] Evaluation of fermion loops applied to the calculation of the η' mass and the nucleon scalar and electromagnetic form factors, Comput.Phys.Commun. **183**, 1215 (2012), 1108.2473.
[67] A. Airapetian et al. (HERMES Collaboration), Phys.Rev. **D75**, 012007 (2007), hep-ex/0609039.
[68] D. Arndt and M. J. Savage, Nucl. Phys. **A697**, 429 (2002), nucl-th/0105045.
[69] W. Detmold, W. Melnitchouk, and A. W. Thomas, Phys.Rev. **D66**, 054501 (2002), hep-lat/0206001.
[70] M. Dorati, T. A. Gail, and T. R. Hemmert, Nucl. Phys. **A798**, 96 (2008), nucl-th/0703073.
[71] There was a mistake in the extraction of L^q of Ref. [1] using N_f=2 twisted mass fermions, which is corrected here.

Appendix A: Numerical results for the isovector sector

m_π (GeV) (no. confs)	$(Q)^2$	G_E	G_M	G_A	G_p
$\beta = 1.95$, $32^3 \times 64$					
	0.0	1.000(1)	3.930(117)	1.141(18)	18.211(9.209)
	0.192	0.734(6)	2.979(61)	0.995(14)	9.462(399)
0.354	0.372	0.570(7)	2.355(46)	0.872(12)	6.116(226)
(950)	0.542(1)	0.469(10)	1.937(47)	0.775(14)	4.512(209)
	0.704(1)	0.392(12)	1.676(57)	0.714(21)	3.117(208)
	0.859(2)	0.331(11)	1.405(46)	0.642(18)	2.591(134)
	1.007(2)	0.288(13)	1.250(53)	0.589(21)	2.134(129)
	1.287(3)	0.208(20)	0.950(79)	0.480(39)	1.441(182)
	1.420(4)	0.185(20)	0.865(85)	0.450(41)	1.249(163)
$\beta = 2.10$, $48^3 \times 96$					
	0.0	1.006(6)	3.855(342)	1.164(62)	14.880(11.790)
	0.147	0.722(21)	2.849(198)	1.034(47)	10.454(1.445)
0.210	0.284	0.565(23)	2.347(142)	0.909(42)	6.317(783)
(900)	0.414(1)	0.430(30)	1.950(153)	0.850(52)	5.227(699)
	0.537(1)	0.444(41)	1.622(170)	0.690(68)	2.466(723)
	0.655(2)	0.318(29)	1.338(120)	0.689(53)	2.628(395)
	0.768(3)	0.266(32)	1.291(136)	0.707(71)	2.763(481)
	0.980(4)	0.218(52)	1.104(237)	0.558(129)	2.466(701)
	1.081(5)	0.186(44)	0.686(164)	0.437(110)	1.714(541)

TABLE VII: Results on G_E, G_M, G_A and G_p form factors at $\beta = 1.95$ ($32^3 \times 64$) and $\beta = 2.10$ ($48^3 \times 96$).

m_π (GeV) (no. confs)	$(Q)^2$	A_{20}	B_{20}	$\tilde{A}_{20}$	$\tilde{B}_{20}$
	$\beta = 1.95$, $32^3 \times 64$				
	0.0	0.270(5)	0.344(19)	0.302(5)	0.648(71)
	0.192	0.242(4)	0.292(15)	0.281(5)	0.582(121)
0.354	0.372	0.222(4)	0.266(15)	0.264(5)	0.578(65)
(950)	0.542(1)	0.207(5)	0.266(15)	0.249(6)	0.495(73)
	0.704(1)	0.195(6)	0.213(20)	0.231(7)	0.236(81)
	0.859(2)	0.177(6)	0.209(15)	0.219(7)	0.319(46)
	1.007(2)	0.163(8)	0.192(16)	0.202(9)	0.294(47)
	1.287(3)	0.152(14)	0.169(25)	0.170(15)	0.200(63)
	1.420(4)	0.134(14)	0.134(21)	0.164(16)	0.165(53)
	$\beta = 2.10$, $48^3 \times 96$				
	0.0	0.228(18)	0.205(62)	0.251(19)	0.518(251)
	0.147	0.206(14)	0.184(63)	0.242(14)	0.793(475)
0.210	0.284	0.190(12)	0.233(52)	0.247(14)	0.830(244)
(900)	0.414(1)	0.165(16)	0.224(58)	0.229(18)	0.526(259)
	0.537(1)	0.176(23)	0.159(63)	0.204(25)	-0.446(289)
	0.655(2)	0.152(16)	0.159(49)	0.180(19)	-0.036(145)
	0.768(3)	0.167(20)	0.205(53)	0.181(24)	0.101(160)
	0.980(4)	0.173(40)	0.305(90)	0.164(43)	0.371(233)
	1.081(5)	0.142(33)	0.164(65)	0.122(35)	0.106(166)

TABLE VIII: Results on A_{20}, B_{20}, $\tilde{A}_{20}$ and $\tilde{B}_{20}$ form factors at $\beta = 1.95$ ($32^3 \times 64$) and $\beta = 2.10$ ($48^3 \times 96$).

Appendix B: Expressions for the chiral extrapolation of the quark spin and angular momentum

In this Appendix we collect the expression used to extrapolate our lattice data for the quark spin to the physical point. Throughout, we use $\lambda^2 = 1$ GeV^2, $f_\pi = 0.0924$ GeV and $g_A = 1.267$.

In HBχPT the expressions for $A_{20}(0)$ and $B_{20}(0)$ for the isovector combination are given by

$$A_{20}^{I=1}(0) = A_{20}^{I=1(0)} \left\{ 1 - \frac{m_\pi^2}{(4\pi f_\pi)^2} \left[(3g_A^2 + 1) \ln \frac{m_\pi^2}{\lambda^2} + 2g_A^2 \right] \right\} + A_{20}^{I=1(2,m)} m_\pi^2 \tag{29}$$

$$B_{20}^{I=1}(0) = B_{20}^{I=1(0)} \left\{ 1 - \frac{m_\pi^2}{(4\pi f_\pi)^2} \left[(2g_A^2 + 1) \ln \frac{m_\pi^2}{\lambda^2} + 2g_A^2 \right] \right\} + A_{20}^{I=1(0)} \frac{m_\pi^2 g_A^2}{(4\pi f_\pi)^2} \ln \frac{m_\pi^2}{\lambda^2} + B_{20}^{I=1(2,m)} m_\pi^2 \tag{30}$$

$$\tag{31}$$

and for the isoscalar by

$$A_{20}^{I=0}(0) = A_{20}^{I=0(0)} + A_{20}^{I=0(2,m)} m_\pi^2 \tag{32}$$

$$B_{20}^{I=0}(0) = B_{20}^{I=0(0)} \left[1 - \frac{3g_A^2 m_\pi^2}{(4\pi f_\pi)^2} \ln \frac{m_\pi^2}{\lambda^2} \right] - A_{20}^{I=0(0)} \frac{3g_A^2 m_\pi^2}{(4\pi f_\pi)^2} \ln \frac{m_\pi^2}{\lambda^2} + B_{20}^{I=0(2,m)} m_\pi^2 + B_{20}^{I=0(2,\pi)} . \tag{33}$$

The spin carried by the quarks is given by the axial coupling g_A or $\tilde{A}_{10}(0)$ as

$$\Delta\Sigma^{u+d} = \tilde{A}_{10}^{u+d} = \tilde{A}_{10}^{I=0}(0) \tag{34}$$

$$\Delta\Sigma^{u-d} = \tilde{A}_{10}^{u-d} = \tilde{A}_{10}^{I=1}(0) . \tag{35}$$

The corresponding expressions for $\tilde{A}_{10}(0)$ in the isoscalar and isovector cases are

$$\tilde{A}_{10}^{I=1}(0) = \tilde{A}_{10}^{I=1(0)}\left\{1-\frac{m_\pi^2}{(4\pi f_\pi)^2}\left[(2g_A^2+1)\ln\frac{m_\pi^2}{\lambda^2}+g_A^2\right]\right\}+\tilde{A}_{10}^{I=1(2,m)}m_\pi^2 \tag{36}$$

$$\tilde{A}_{10}^{I=0}(0) = \tilde{A}_{10}^{I=0(0)}\left\{1-\frac{3g_A^2m_\pi^2}{(4\pi f_\pi)^2}\left[\ln\frac{m_\pi^2}{\lambda^2}+1\right]\right\}+\tilde{A}_{10}^{I=0(2,m)}m_\pi^2\,. \tag{37}$$

For the total spin J we have

$$J^{I=0} = a_0^{IS}\left[1-\frac{3g_A^2m_\pi^2}{(4\pi f_\pi)^2}\ln\frac{m_\pi^2}{\lambda^2}\right]+a_1^{IS}m_\pi^2+a_2^{IS} \tag{38}$$

$$J^{I=1} = a_0^{IV}\left[1-\frac{m_\pi^2}{(4\pi f_\pi)^2}\left((2g_A^2+1)\ln\frac{m_\pi^2}{\lambda^2}+2g_A^2\right)\right]+a_1^{IV}m_\pi^2 \tag{39}$$

and the expression for $\Delta\Sigma^q$, L^q and J^q are of the form

$$Q^{u,d} = a_2^{u,d}+a_1^{u,d}m_\pi^2+a_0^{u,d}\frac{m_\pi^2}{(4\pi f_\pi)^2}\ln\frac{m_\pi^2}{\lambda^2} \tag{40}$$

where $Q = J, \Delta\Sigma, L$.

We also use covariant baryon chiral perturbation theory (CBχPT) for $A_{20}(0)$, $B_{20}(0)$, $C_{20}(0)$ in the isovector case

$$\begin{aligned}
A_{20}^{I=1}(0) &= a_{20}^v+\frac{a_{20}^vm_\pi^2}{(4\pi f_\pi)^2}\left[-(3g_A^2+1)\ln\frac{m_\pi^2}{\lambda^2}-2g_A^2+g_A^2\frac{m_\pi^2}{m_N^{0\,2}}\left(1+3\ln\frac{m_\pi^2}{m_N^{0\,2}}\right)\right.\\
&- \left.\frac{1}{2}g_A^2\frac{m_\pi^4}{m_N^{0\,4}}\ln\frac{m_\pi^2}{m_N^{0\,2}}+g_A^2\frac{m_\pi}{\sqrt{4m_N^{0\,2}-m_\pi^2}}\left(14-8\frac{m_\pi^2}{m_N^{0\,2}}+\frac{m_\pi^4}{m_N^{0\,4}}\right)arccos\left(\frac{m_\pi}{2m_N^0}\right)\right]\\
&+ \frac{\Delta a_{20}^v(0)g_Am_\pi^2}{3(4\pi f_\pi)^2}\left[2\frac{m_\pi^2}{m_N^{0\,2}}\left(1+3\ln\frac{m_\pi^2}{m_N^{0\,2}}\right)-\frac{m_\pi^4}{m_N^{0\,4}}\ln\frac{m_\pi^2}{m_N^{0\,2}}+\frac{2m_\pi(4m_N^{0\,2}-m_\pi^2)^{\frac{3}{2}}}{m_N^{0\,4}}\right.\\
&\times \left.\arccos\left(\frac{m_\pi}{2m_N^0}\right)\right]+4m_\pi^2\frac{c_8^{(\lambda)}}{m_N^{0\,2}}+\mathcal{O}(p^3)
\end{aligned} \tag{41}$$

$$\begin{aligned}
B_{20}^{I=1}(0) &= b_{20}^v\frac{m_N(m_\pi)}{m_N^0}+\frac{a_{20}^vg_A^2m_\pi^2}{(4\pi f_\pi)^2}\left[\left(3+\ln\frac{m_\pi^2}{m_N^{0\,2}}\right)-\frac{m_\pi^2}{m_N^{0\,2}}\left(2+3\ln\frac{m_\pi^2}{m_N^{0\,2}}\right)\right.\\
&+ \left.\frac{m_\pi^4}{m_N^{0\,4}}\ln\frac{m_\pi^2}{m_N^{0\,2}}-\frac{2m_\pi}{\sqrt{4m_N^{0\,2}-m_\pi^2}}\left(5-5\frac{m_\pi^2}{m_N^{0\,2}}+\frac{m_\pi^4}{m_N^{0\,4}}\right)\arccos\left(\frac{m_\pi}{2m_N^0}\right)\right]+\mathcal{O}(p^3)
\end{aligned} \tag{42}$$

$$\begin{aligned}
C_{20}^{I=1}(0) &= c_{20}^v\frac{m_N(m_\pi)}{m_N^0}+\frac{a_{20}^vg_A^2m_\pi^2}{12(4\pi f_\pi)^2}\left[-1+2\frac{m_\pi^2}{m_N^{0\,2}}\left(1+\ln\frac{m_\pi^2}{m_N^{0\,2}}\right)\right.\\
&- \left.\frac{m_\pi^4}{m_N^{0\,4}}\ln\frac{m_\pi^2}{m_N^{0\,2}}+\frac{2m_\pi}{\sqrt{4m_N^{0\,2}-m_\pi^2}}\left(2-4\frac{m_\pi^2}{m_N^{0\,2}}+\frac{m_\pi^4}{m_N^{0\,4}}\right)\arccos\left(\frac{m_\pi}{2m_N^0}\right)\right]+\mathcal{O}(p^3)
\end{aligned} \tag{43}$$

and the isoscalar case

$$
\begin{aligned}
A_{20}^{I=0}(0) &= a_{20}^s + 4m_\pi^2 \frac{c_9}{m_N^{0\,2}} - \frac{3a_{20}^s g_A^2 m_\pi^2}{(4\pi f_\pi)^2}\left[\frac{m_\pi^2}{m_N^{0\,2}} + \frac{m_\pi^2}{m_N^{0\,2}}\left(2 - \frac{m_\pi^2}{m_N^{0\,2}}\right)\ln\frac{m_\pi}{m_N^0}\right. \\
&+ \left.\frac{m_\pi}{\sqrt{4m_N^{0\,2} - m_\pi^2}}\left(2 - 4\frac{m_\pi^2}{m_N^{0\,2}} + \frac{m_\pi^4}{m_N^{0\,4}}\right)\arccos\left(\frac{m_\pi}{2m_N^0}\right)\right] + \mathcal{O}(p^3) \qquad (44) \\
B_{20}^{I=0}(0) &= b_{20}^s \frac{m_N(m_\pi)}{m_N^0} - \frac{3a_{20}^s g_A^2 m_\pi^2}{(4\pi f_\pi)^2}\left[\left(3 + \ln\frac{m_\pi^2}{m_N^{0\,2}}\right) - \frac{m_\pi^2}{m_N^{0\,2}}\left(2 + 3\ln\frac{m_\pi^2}{m_N^{0\,2}}\right)\right. \\
&+ \left.\frac{m_\pi^4}{m_N^{0\,4}}\ln\frac{m_\pi^2}{m_N^{0\,2}} - \frac{2m_\pi}{\sqrt{4m_N^{0\,2} - m_\pi^2}}\left(5 - 5\frac{m_\pi^2}{m_N^{0\,2}} + \frac{m_\pi^4}{m_N^{0\,4}}\right)\arccos\left(\frac{m_\pi}{2m_N^0}\right)\right] \qquad (45) \\
C_{20}^{I=0}(0) &= c_{20}^s \frac{m_N(m_\pi)}{m_N^0} - \frac{a_{20}^s g_A^2 m_\pi^2}{4(4\pi f_\pi)^2}\left[-1 + 2\frac{m_\pi^2}{m_N^{0\,2}}\left(1 + \ln\frac{m_\pi^2}{m_N^{0\,2}}\right)\right. \\
&- \left.\frac{m_\pi^4}{m_N^{0\,4}}\ln\frac{m_\pi^2}{m_N^{0\,2}} + \frac{2m_\pi}{\sqrt{4m_N^{0\,2} - m_\pi^2}}\left(2 - 4\frac{m_\pi^2}{m_N^{0\,2}} + \frac{m_\pi^4}{m_N^{0\,4}}\right)\arccos\left(\frac{m_\pi}{2m_N^0}\right)\right] . \qquad (46)
\end{aligned}
$$

We then extract the total spins using

$$
\begin{aligned}
J^{u+d} &= \frac{1}{2}\left(A_{20}^{I=0}(0) + B_{20}^{I=0}(0)\right) \\
J^{u-d} &= \frac{1}{2}\left(A_{20}^{I=1}(0) + B_{20}^{I=1}(0)\right) . \qquad (47)
\end{aligned}
$$